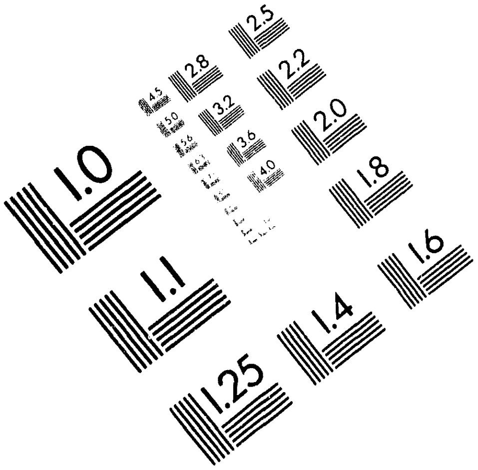

AIIM

Association for Information and Image Management

1100 Wayne Avenue, Suite 1100
Silver Spring, Maryland 20910
301/587-8202

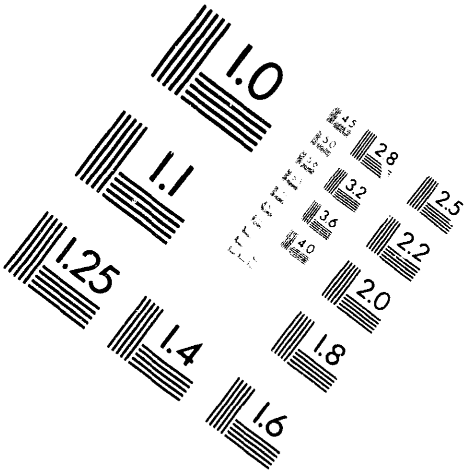

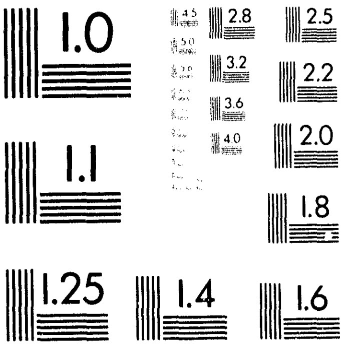

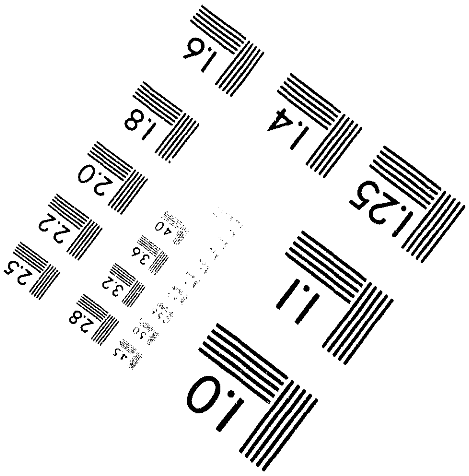

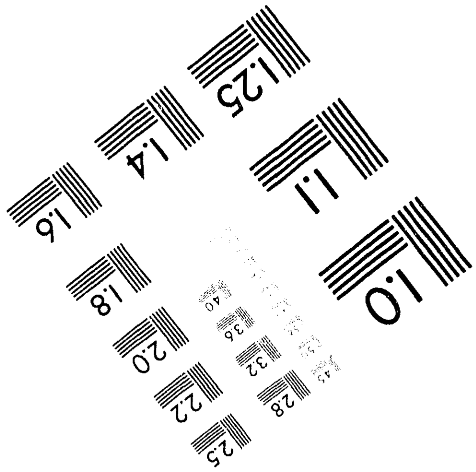

MANUFACTURED TO AIIM STANDARDS
BY APPLIED IMAGE, INC.

1 of 1

10/5-17-94 JS ①

SANDIA REPORT

SAND94-0129 • UC-705
Unlimited Release
Printed April 1994

Micromechanical Modeling of Advanced Materials

S. A. Silling, P. A. Taylor, J. L. Wise, M. D. Furnish

Prepared by
Sandia National Laboratories
Albuquerque, New Mexico 87185 and Livermore, California 94550
for the United States Department of Energy
under Contract DE-AC04-94AL85000

Approved for public release; distribution is unlimited.

Issued by Sandia National Laboratories, operated for the United States Department of Energy by Sandia Corporation.

Printed in the United States of America. This report has been reproduced directly from the best available copy.

Available to DOE and DOE contractors from
Office of Scientific and Technical Information
PO Box 62
Oak Ridge, TN 37831

Prices available from (615) 576-8401, FTS 626-8401

Available to the public from
National Technical Information Service
US Department of Commerce
5285 Port Royal Rd
Springfield, VA 22161

NTIS price codes
Printed copy: A04
Microfiche copy: A01

SAND94-0129
Unlimited Release
Printed April 1994

Distribution
UC-705

MICROMECHANICAL MODELING OF ADVANCED MATERIALS

S. A. Silling, P. A. Taylor,
Computational Physics and Mechanics Department

J. L. Wise,
Geothermal Research Department
and
M. D. Furnish
Experimental Impact Physics Department

Sandia National Laboratories
Albuquerque, NM 87185-0820

Abstract

Funded as a laboratory-directed research and development (LDRD) project, the work reported here focuses on the development of a computational methodology to determine the dynamic response of heterogeneous solids on the basis of their composition and microstructural morphology. Using the solid dynamics wavecode CTH, material response is simulated on a scale sufficiently fine to explicitly represent the material's microstructure. Conducting "numerical experiments" on this scale, we explore the influence that the microstructure exerts on the material's overall response. These results are used in the development of constitutive models that take into account the effects of microstructure *without* explicit representation of its features. Applying this methodology to a glass-reinforced plastic (GRP) composite, we examined the influence of various aspects of the composite's microstructure on its response in a loading regime typical of impact and penetration. As a prerequisite to the microscale modeling effort, we conducted extensive materials testing on the constituents, S-2 glass and epoxy resin (UF-3283), obtaining the first Hugoniot and spall data for these materials. The results of this work are used in the development of constitutive models for GRP materials in transient-dynamics computer wavecodes.

Acknowledgments

The authors are indebted to John H. Gieske (2752) for his careful ultrasonic characterization of the test components, and to Ernest D. Apodaca and Johnny A. Moya (2481-3) for lapping the target and impactor plates. The competent implementation of the experiments by David E. Cox (1433) is also greatly appreciated. Special thanks are owed to David M. Miller and Patrick F. Aubourg, Owens-Corning Fiberglas Corporation, for preparing and supplying the necessary high-quality bulk samples of S-2 glass.

Contents

Figures

Tables

Intentionally Left Blank

1. Introduction

This report summarizes the work performed for the laboratory-directed research and development (LDRD) project entitled “Micromechanical Modeling of Advanced Materials.” The objective of this work was to develop a computational methodology for determining the dynamic response of heterogeneous solids on the basis of their composition and microstructural morphology. Using a transient solid dynamics wavecode, we simulate the dynamic response of a heterogeneous material on a scale fine enough to explicitly represent the material’s microstructure. By conducting “numerical experiments” on this scale, we explore the influence that the microstructure exerts on the material’s overall response. The results of such simulations support the development of constitutive models that take into account the effects of microstructure *without* explicit representation of its features. In general, this approach is applicable to many types of composites and porous materials.

For illustrative purposes, we focus on a specific class of heterogeneous material, namely continuous-fiber reinforced composites. In particular, we choose a composite consisting of S-2 glass fiber reinforcing an epoxy matrix. Currently, this composite, referred to as a glass-reinforced plastic, or GRP, is of significant interest to the defense community for applications involving ballistic protection of certain armored vehicles from small metal fragments moving at velocities on the order of 1 km/sec. This sort of application has motivated both our choice of composite material and the conditions under which the mechanical response of the material is investigated.

In this report, we describe our efforts to simulate the response of glass-reinforced epoxy composites in a regime involving large pressures and shear strains typically experienced by these materials when undergoing impact and penetration by a high-speed projectile. These simulations are conducted at the microscale level, where we study the influence of the material’s microstructure on its response to well-defined pressure/shear stress histories. In particular, we demonstrate the influence of two microstructural aspects: the volume fraction of reinforcing material, and the bonding strength between the reinforcing and matrix constituents (i.e., between the glass and epoxy). These two aspects have been identified in various ballistic performance studies (Bless, et al. 1985; Vasudev, et al. 1987) as having a significant influence on the composite’s ability to resist penetration. However, those studies were empirical in nature with no attempt made to analyze the mechanics of the penetration process. With the methodology we have developed in this project, we can, for example, further the development of constitutive models that will permit a detailed analysis of the penetration process in GRP composites and their dependence on the reinforcement volume fraction and the constituent bonding strength.

To accurately model the microscale response of any composite, our methodology requires a knowledge of the equation-of-state and constitutive models of strength and failure for each constituent. In the case of the S-2 glass and epoxy materials comprising our chosen composite system, this information was not readily available in the literature. Consequently, we conducted experimental studies on the glass and epoxy constituents, measuring the dynamic response of these materials for the construction of equation-of-state and constitutive models.

The primary analytical tool used in this study was the CTH wavecode (McGlaun, et al. 1990). CTH is an Eulerian wavecode designed to simulate continuum mechanics problems involving large deformations at high strain-rates which typically occur in problems involving impact and penetration. For this project, the CTH code was modified to (1)-allow a large number of material inclusions to be embedded in a matrix material (to construct the composite sample), (2)-accurately prescribe either deformation or stress histories on the sample, and (3)-compute the average material response of the composite sample. A detailed description of these modifications is included in this report.

The significance of the methodology described here centers on the ability to perform "numerical experiments" that allow one to construct continuum models for heterogeneous materials using only the material properties of the constituents making up the composite. That is, we use an approach that predicts the response of a composite material in the absence of any knowledge of the properties of the composite. This approach circumvents a costly, if tractable, experimental investigation to explore the influence of numerous microstructural and morphological aspects of a heterogeneous material under dynamic conditions. In fact, with the methodology we employ, once the constituent properties are known, the remaining experimental work can focus on tests that provide data for validation of the resulting constitutive models.

2. Approach

The project involved both experimental and analytical work. The experimental effort focused on obtaining constituent material properties and, if time and funding permitted, on conducting tests on glass/epoxy composites possessing various reinforcement lay-ups to validate the microscale results. The constituent properties were determined from data collected during ultrasonic, split Hopkinson pressure bar, and gas/powder gun experiments that provided elastic, plastic, and impact/spall data up to 170 Kbars for the glass and 140 Kbars for epoxy. Due to budgetary constraints, however, we were unable to achieve the goal of collecting dynamic response data on composite samples.

The numerical work started with the development of modifications to CTH that permitted us to conduct and analyze microscale simulations on continuous-fiber reinforced composites. Once in place, this software was used to perform numerical experiments on the composite system of our choice.

As mentioned earlier, for illustrative purposes, we chose a specific composite system to study, namely, a glass/epoxy composite that was already of interest to the armor applications community. In particular, the composite consists of an S-2 glass procured from Owens-Corning Fiberglas Corporation reinforcing an epoxy resin (UF-3283 adhesive) supplied by Thiokol Corporation. Each of these materials is currently in use in a variety of aerospace and defense applications.

Section 3 contains the results of the experimental work aimed at determining the material properties of the glass and epoxy constituents. The results reported there are significant in their own right since they constitute the first investigation into the impact responses of both the S-2 glass and the UF-3283 epoxy resin.

Section 4 provides a detailed description of the computer codes used to simulate composite material response on a microscale.

Section 5 presents the results of a series of numerical experiments aimed at providing an understanding of the dynamic response of uniaxial reinforced glass/epoxy composites in a two-dimensional, plane-strain setting. These results clearly demonstrate the influence that the glass volume fraction and constituent bonding strength exert on the strength and failure response of the composite in planes perpendicular to the reinforcement direction. This section is completed with the demonstration of the code's ability to predict the dynamic response of the composite in three-dimensions.

Section 6 concludes the report with a summary of the work performed for the project, its significance, and suggested directions for further work.

3. Experimental Results on Constituent Materials

3.1 S-2 Glass

In this section, we describe a series of plate-impact experiments which provide time-resolved data characterizing the dynamic mechanical behavior of Owens-Corning type S-2 glass. This glass is used in fiber form as the reinforcing constituent of the glass/epoxy composite system. The experiments described in this section were performed on the single-stage propellant (powder) gun operated at the Sandia STAR facility. In these tests, a velocity interferometer system, VISAR (L. M. Barker, et al. 1972), acquired wave-profile data for bulk samples of S-2 glass which were specially produced in plate form by the Owens-Corning Fiberglas Corporation. The test geometry and resultant particle-velocity histories are summarized in the present section along with pertinent experimental parameters and pre-test material properties data. To our knowledge, the experimental data reported here is the first obtained on the impact response of type S-2 glass.

3.1.1 Experimental Configuration

The six tests reported herein (designated S2G1, 2, 3, 4, 5, 6) employed target assemblies designed for one-dimensional (uniaxial strain) impact loading of S-2 glass target plates. The test configuration is illustrated in Figure 3.1.1. In three of the tests (S2G1, 2, 3), the VISAR monitored the velocity of the rear free surface of the glass target, which was coated with a reflective thin film. For the remaining tests (S2G4, 5, 6), a PMMA window was

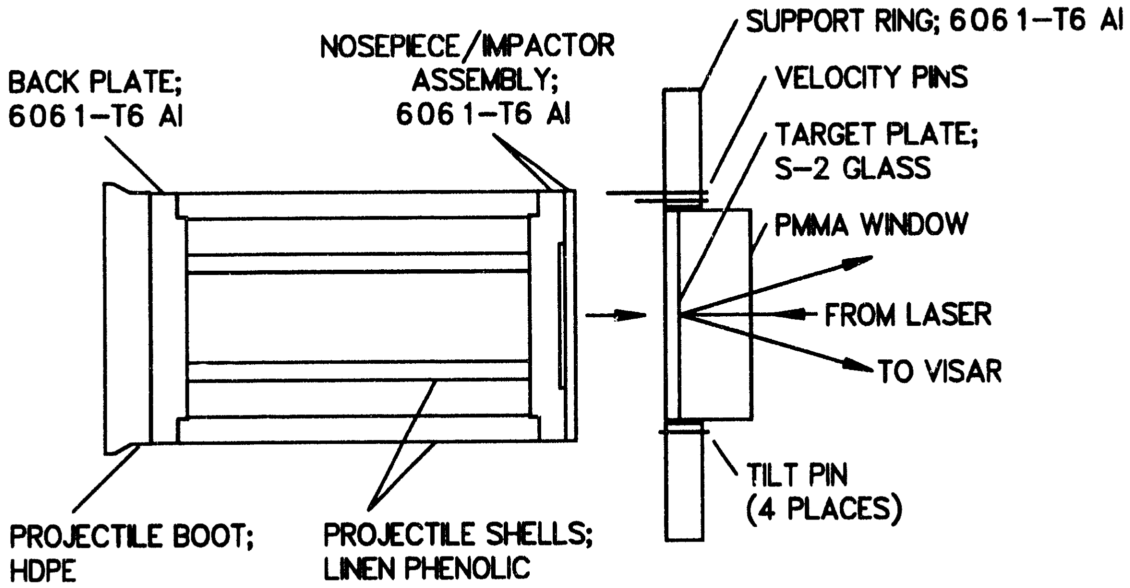

Figure 3.1.1. Experimental configuration for impact tests on type S-2 glass.

bonded to the rear surface of the glass. A reflective coating on the forward surface of the PMMA window allowed VISAR detection of the glass/PMMA interface velocity. In each test, a 6061-T6 aluminum impactor plate provided the initial loading of the glass through a right-going compressional wave, followed by unloading through a right-going rarefaction originating at the impactor rear surface. Interaction within the glass of this right-going rarefaction with the initial left-going rarefaction, originating at the rear surface of the glass, produced tensile stresses suitable for evaluation of the spall strength of the glass. In the experiments involving PMMA windows, the low shock impedance of PMMA relative to glass assured the generation of a left-going rarefaction in the S-2 glass upon arrival of the initial right-going compression at the glass/PMMA interface.

The six glass samples were fabricated as flat circular target plates, nominally 5-mm thick and 73.7-mm in diameter. An epoxy bond around the target-plate periphery held the glass concentrically within a standard support ring (12.7-mm thick; 158.8-mm outer diameter; 76.2-mm inner diameter) machined from 6061-T6 aluminum. The impact surface of the glass was flush with the front face of this ring. Final machined dimensions of the glass plates and PMMA windows are reported in Table 3.1.1.

Table 3.1.1: Summary of Parameters for Impact Tests on S-2 Glass.

Shot Number	Impact Velocity (km/sec)	S-2 Glass Target Thickness/ Diameter (mm)	PMMA Window Thickness/ Diameter (mm)	6061-T6 Al Impactor Thickness/ Diameter (mm)
1	0.576	4.763/ 73.72	---	3.616/ 88.03
2	0.524	4.971/ 73.73	---	3.612/ 88.06
3	0.959	4.962/ 73.72	---	3.608/ 88.01
4	1.513	4.728/ 73.72	25.03/ 73.79	3.603/ 88.02
5	2.289	5.010/ 73.73	25.58/ 73.74	3.620/ 88.04
6	0.960	5.020/ 73.72	25.10/ 73.67	3.608/ 88.04

Dynamic loading of the S-2 glass was produced by the impact of a flat-faced projectile that was accelerated to a preselected velocity by the powder gun. The forward element of the projectile assembly consisted of a 6061-T6 aluminum impactor plate which was nominally 3.6-mm thick by 88.0-mm in diameter. The impactor was bonded to a projectile nosepiece (also 6061-T6 aluminum) which had a 2.0-mm deep by 50.8-mm diameter counterbore in its front face that left the central portion of the impactor unsupported. This arrangement caused the formation of the initial right-going rarefaction wave that was transmitted into the glass target. Final machined dimensions of the impactor are compiled in Table 3.1.1. Measurements of impact velocity, also recorded in Table 3.1.1, were obtained by means of coaxial shorting pins mounted in the target support ring.

For all experiments, the particle-velocity history at the glass rear surface was measured using a velocity interferometer system, VISAR, with an argon-ion laser light source (wavelength = 514.5 nm). Estimated temporal resolution for this system was approximately 3 nsec. The interferometer sensitivity was 0.2528 (km/sec)/fringe for shots S2G1 and 2, 0.4028 (km/sec)/fringe for shots S2G3 and 4, 0.5518 (km/sec)/fringe for shot S2G5, and 0.3041 (km/sec)/fringe for shot S2G6. Consequently, given an estimated uncertainty of ±0.02 for the VISAR fringe count (L. M. Barker, et al. 1972), the corresponding uncertainty in the reported particle-velocity data was ±0.005 km/sec for shots S2G1 and 2, ±0.008 km/sec for shots S2G3 and 4, ±0.011 km/sec for shot S2G5, and ±0.006 km/sec for shot S2G6.

3.1.2 Pre-Shot Characterization of Test Materials

Density and ultrasonic wave-speed measurements were made for each glass target plate, PMMA window, and aluminum impactor; the resultant mean values for these components are recorded in Table 3.1.2. The density estimates were based on component weights (corrected for atmospheric buoyancy) and the thickness and diameter dimensions listed in Table 3.1.1. The measured densities of the six S-2 glass samples agreed with one another to within 0.2%, and the mean S-2 glass density (2.492 g/cm^3) was within 0.04% of the upper end of the range reported by the manufacturer (2.464-2.491 g/cm^3) for S-2 glass fiber (Owens-Corning Fiberglas Corporation 1990). The mean densities of the six 6061-T6 aluminum impactors (2.699 g/cm^3) and the three PMMA windows (1.185 g/cm^3) were slightly lower than values (2.703 and 1.186 g/cm^3, respectively) which have been given elsewhere

Table 3.1.2: Average Material Properties of S-2 Glass.

Test Component	Initial Density, ρ_0 (g/cm^3)	Longitudinal Wave Speed, C_L (km/sec)	Shear Wave Speed, C_S (km/sec)	Bulk Wave Speed, C_0 (km/sec)	Poisson's Ratio, ν
S-2 Glass Target	2.492	6.676	3.913	4.914	0.2383
PMMA Window	1.185	2.752	1.389	2.236	0.3291
6061-T6 Aluminum Impactor	2.699	6.409	3.174	5.258	0.3375

(Los Alamos National Laboratory 1980) for these two materials.

Both longitudinal, C_L, and shear, C_S, wave speeds were measured for all components using ultrasonic techniques. For the glass and aluminum samples, driving frequencies of 20 and 5 MHz were used, respectively, for the longitudinal and shear wave measurements. For the PMMA samples, frequencies of 2.25 and 1.0 MHz were used. Mean values of C_L and C_S for each material are listed in Table 3.1.2 along with calculated values for the bulk sound speed, C_0, and Poisson's ratio, ν. The sound speed for S-2 glass of 5.852 km/sec reported by the manufacturer differs significantly from the mean values reported here for C_L and C_0 as well as the computed thin rod wave velocity of 6.158 km/sec, calculated from the present data. This discrepancy may be due to differences in measurement technique, or to fundamental differences in the acoustic properties of bulk glass versus fiber samples.

3.1.3 Particle-Velocity Measurements

The individual velocity histories obtained for shots S2G1, 2, 3, 4, 5, and 6 are shown, respectively, in Figures 3.1.2 through 3.1.7 where time t = 0.0 μsec corresponds to first contact of the impactor with the glass target. The VISAR interference-fringe signals and beam-intensity level were captured by LeCroy waveform digitizers. For all experiments, the VISAR records initially indicated a finite-risetime compressional loading. The arrival time of the leading break, or "toe," of this wavefront has been assigned on the basis of the measured glass thickness for a particular test (Table 3.1.1) and the mean C_L value determined for the six S-2 glass samples (Table 3.1.2).

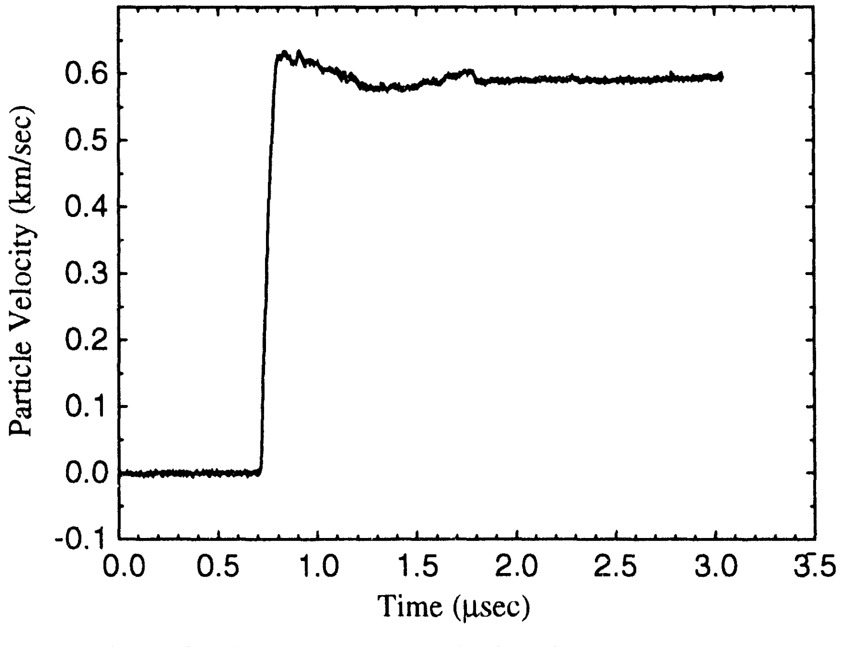

Figure 3.1.2. Free-surface velocity history for shot S2G1.

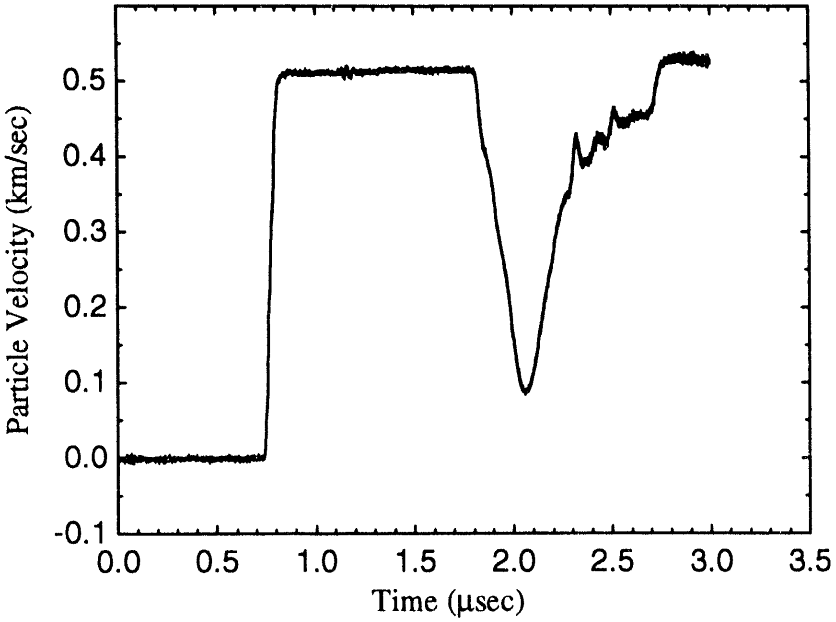

Figure 3.1.3. Free-surface velocity history for shot S2G2.

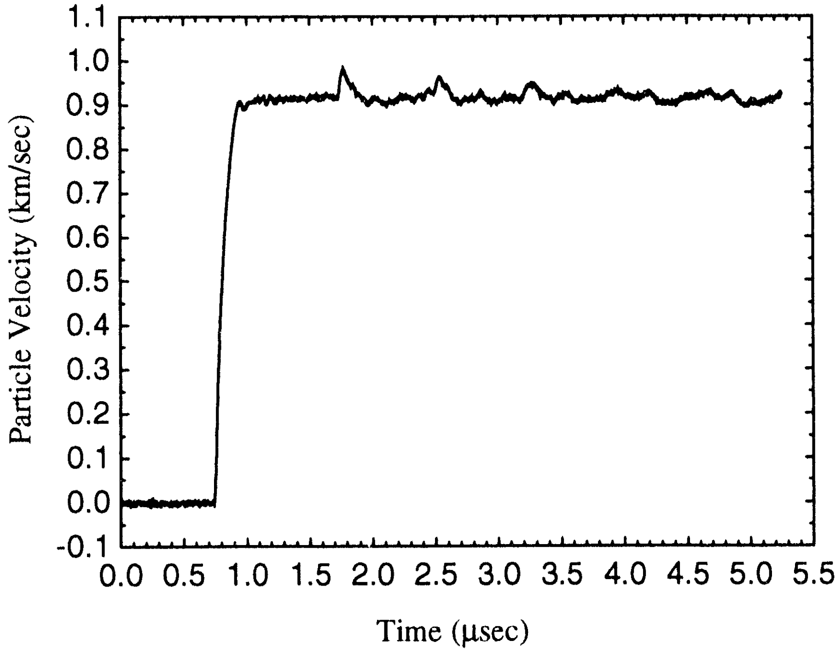

Figure 3.1.4. Free-surface velocity history for shot S2G3.

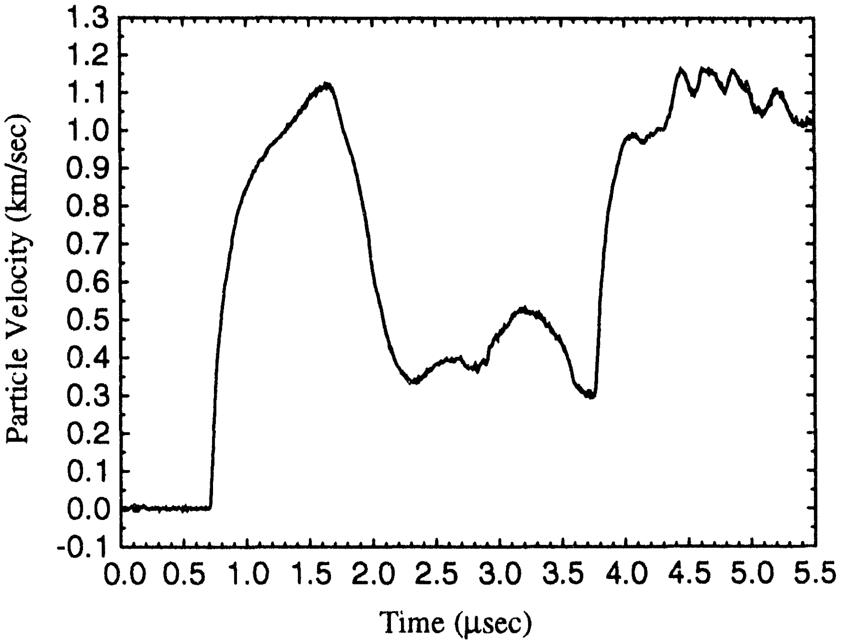

Figure 3.1.5. Target/window interface velocity history for shot S2G4.

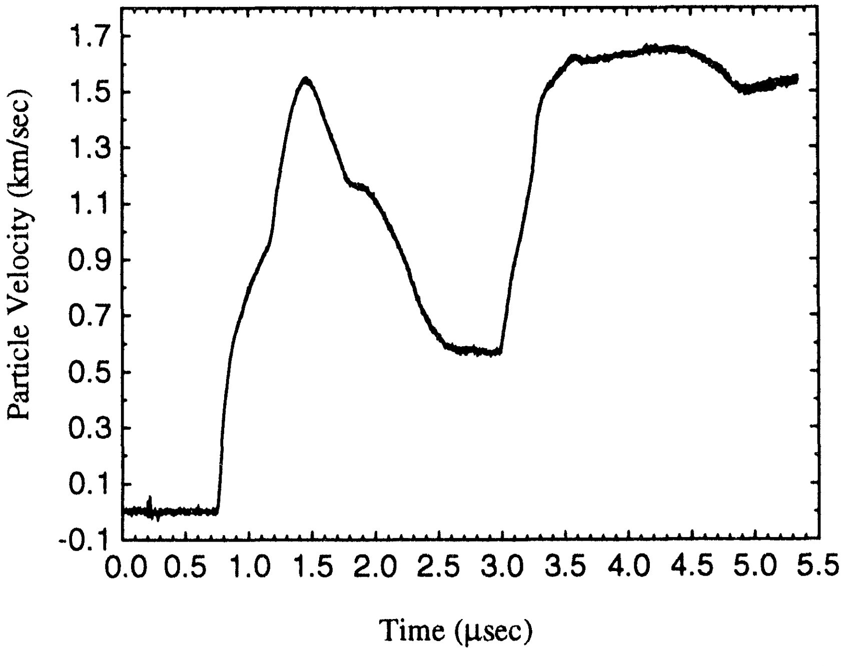

Figure 3.1.6. Target/window interface velocity history for shot S2G5.

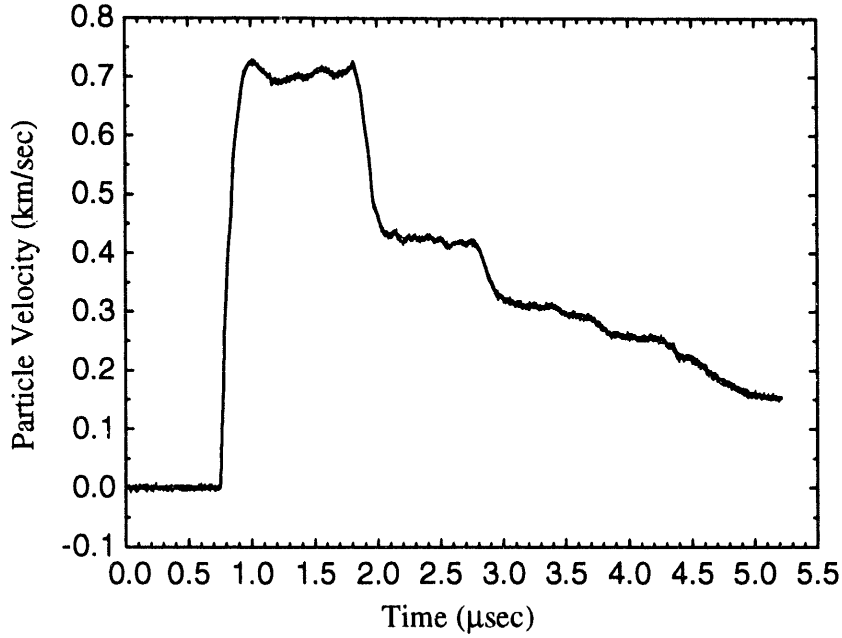

Figure 3.1.7. Target/window interface velocity history for shot S2G6.

For comparison, the overall wave profiles obtained for shots S2G1, 2, and 3, which did not involve PMMA windows, are plotted together in Figure 3.1.8. The strong release/pullback signal evident in the record for shot S2G2 indicates that a significant spall strength was maintained through the initial compressive loading. The absence of this signal in the records for shots S2G1 and 3 indicates a loss of spall strength for compressive loading to peak stresses higher than that achieved in shot S2G2.

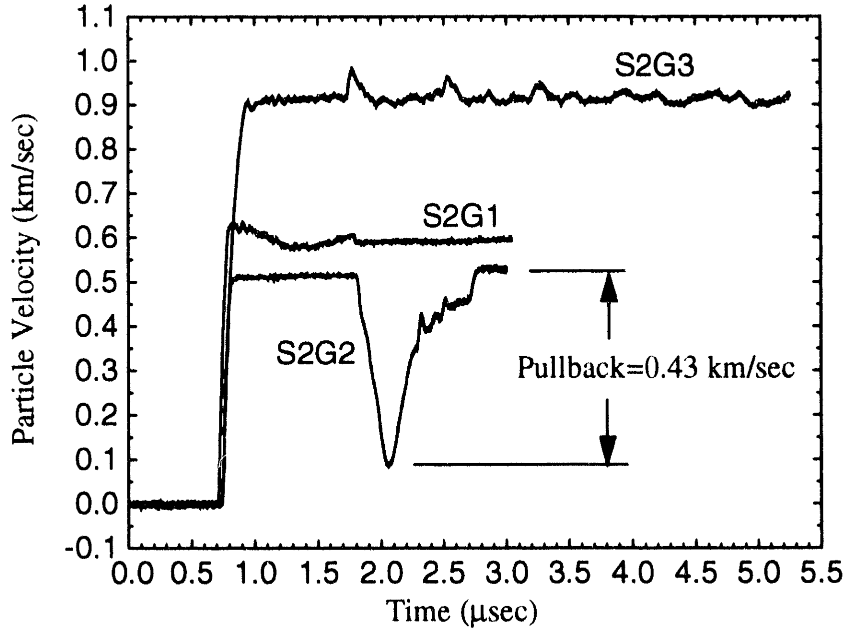

Figure 3.1.8. Comparison of free-surface velocity histories for shots S2G1-3.

Similarly, the overall profiles for shots S2G4, 5, and 6, which included PMMA windows, are plotted together for comparison in Figure 3.1.9. Substantial releases were evident in all three of these records, with subsequent pullbacks (velocity increases) for shots S2G4 and 5.

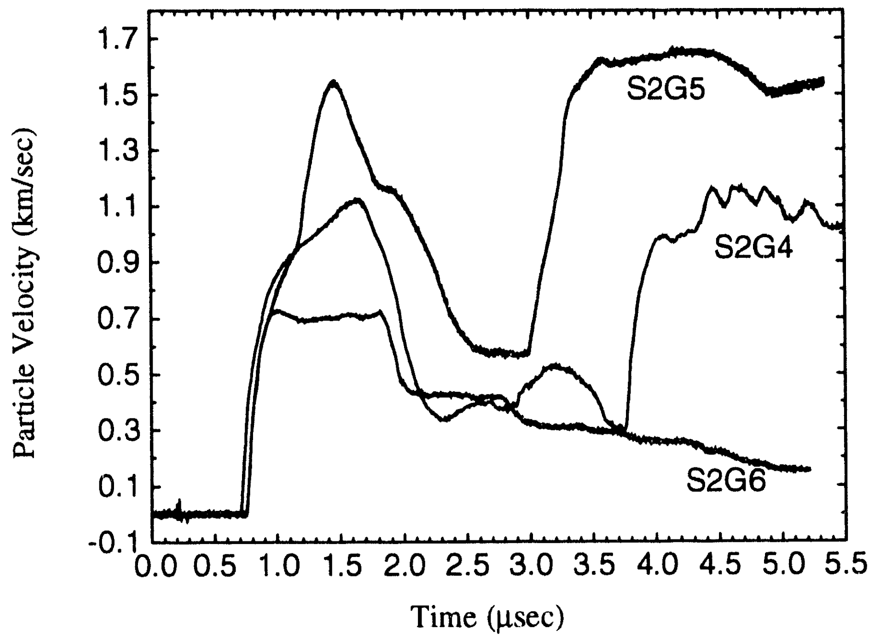

Figure 3.1.9. Comparison of target/window interface velocity histories for shots S2G4-6.

The initial free-surface loading histories for tests S2G1, 2, and 3 (without PMMA windows) are plotted together for comparison in Figure 3.1.10. The finite risetimes of these initial loading histories show the dispersive behavior of the glass as indicated by the absence of shock-front development. Our results suggest that the elastic limit of the S-2 glass was not exceeded during these three low-pressure tests. This result is consistent with recent data obtained from similar impact experiments which were conducted on samples of an aluminosilicate glass (Wise, et al. 1992). However, referring to Figure 3.1.11 where the initial loading/unloading histories for the three high-pressure tests S2G4, 5, and 6 (with PMMA windows) are plotted, the development of a steep secondary compression is observed for impact loading to higher pressures, as indicated by the velocity history of shot S2G5. This two-wave, elastic-plastic loading behavior is similar to that previously reported for fused quartz (Chhabildas, et al. 1983).

3.1.4 Derived Hugoniot and Spall Properties of S-2 Glass

As noted previously, the VISAR records indicated transmission of an initial finite-risetime compressional loading through the glass target in all experiments. The free-surface loading histories for the low pressure tests S2G1, 2, and 3 (without PMMA windows) consistently displayed dispersive behavior with no apparent shock-front development. This dispersive loading-front behavior was also noted for the higher pressure tests S2G4, 5, and 6 (with

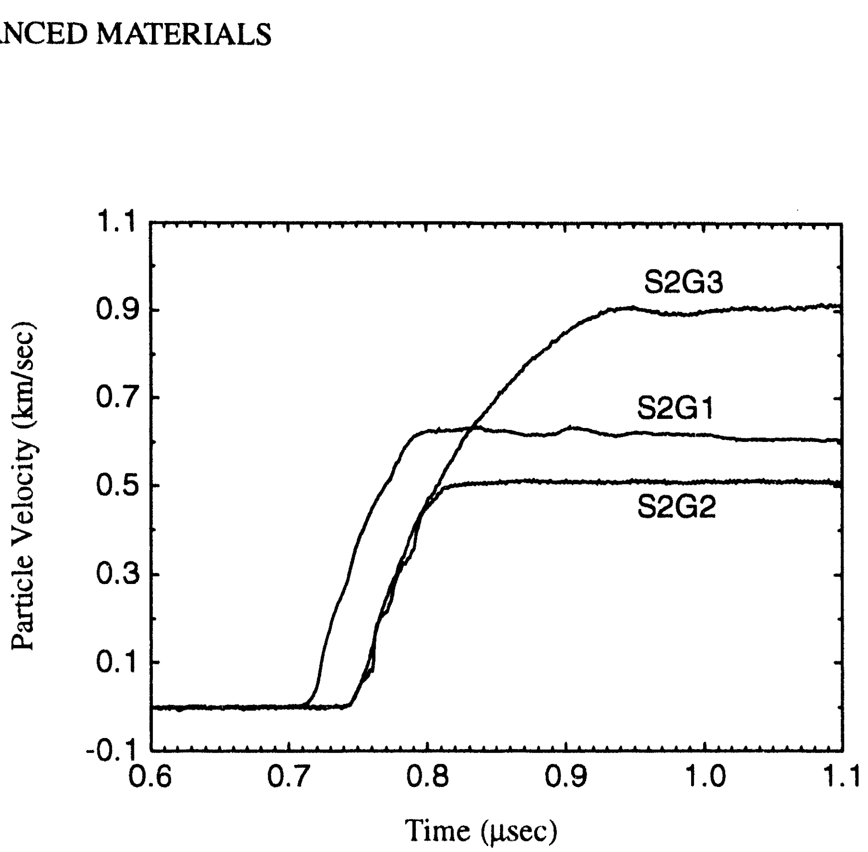

Figure 3.1.10. Initial loading velocity histories for shots S2G1-3.

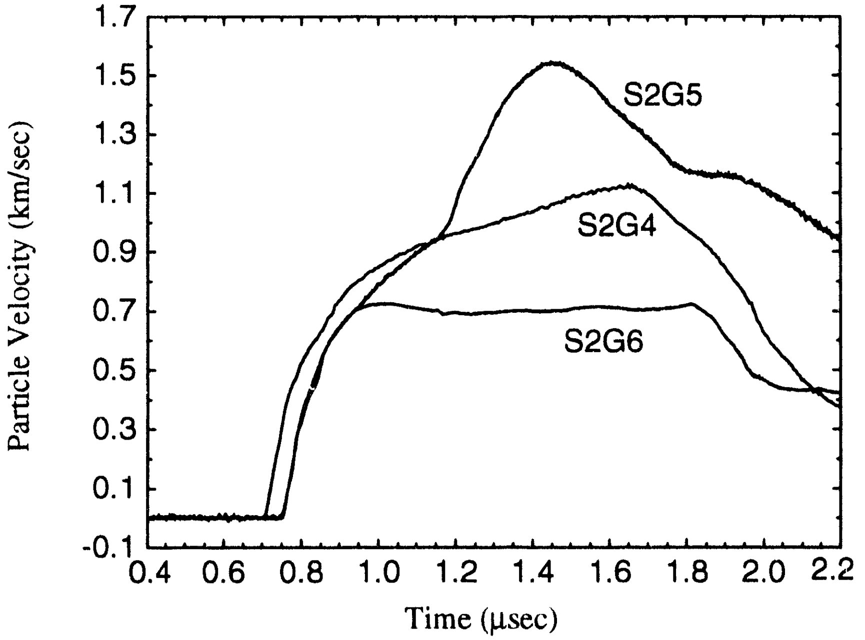

Figure 3.1.11. Initial loading/unloading velocity histories for shots S2G4-6.

PMMA windows). However, the development of a steeper secondary compression was observed for shot S2G5 which involved the highest impact stress.

An impedance-matching determination of Hugoniot parameters for the S-2 glass has been performed using an estimated "shock" velocity for the leading compression. This shock velocity was assigned on the basis of the arrival time of the half-amplitude point on the leading compression relative to the peak particle velocity ultimately attained through the wavefront. Since sharp shocks were not observed in any of the experiments, results obtained with this approach should be considered only as first approximations.

To accomplish an impedance-matching solution, the "shock" velocity estimates were used in conjunction with reported Hugoniot data for 6061-T6 aluminum (Los Alamos National Laboratory 1980) to determine the Hugoniot particle velocity, U_{PH}, and stress, P_H, for S-2 glass. A linear shock-velocity U_S versus particle-velocity U_P relationship of the standard form $U_S = C_0 + sU_P$ was used to model the 6061-T6 aluminum, where $C_0 = 5.35$ km/sec and $s = 1.34$. The resultant U_{PH} and P_H parameters for S-2 glass from shots S2G1 through 6 are listed in Table 3.1.3. Since an equilibrium particle velocity was not obtained through the leading compression for shots S2G4 and S2G5 (see Figures 3.1.5 and 3.1.6), wave attenuation may have occurred in these tests. Consequently, the results listed in Table 3.1.3 for shots S2G4 and S2G5 are subject to additional uncertainty.

Table 3.1.3: Estimated Hugoniot Parameters for S-2 Glass.

Shot Number	U_{PH} (km/sec)	P_H (Kbar)
S2G1	0.284	45.3
S2G2	0.261	40.5
S2G3	0.483	76.9
S2G4	0.816*	118.0*
S2G5	1.34*	170.0*
S2G6	0.488	76.2

* Possible wave attenuation.

In experiments S2G1, 2, and 3, the impactor was sufficiently thin to allow full transmission of the initial right-going rarefaction, originating at the impactor rear surface, into the glass target where it interacted with the initial left-going rarefaction originating at the rear free surface of the glass. For test S2G2 which involved the lowest impact stress, the arrival of the initial rarefaction at the glass free surface is seen in the VISAR record as a period of decreasing velocity (pullback) which began at $t = 1.80$ µsec after impact, and ended with the attainment of a local minimum velocity at $t = 2.07$ µsec (see Figure 3.1.3). The observed change in free-surface velocity, Δu_{fs}, between the peak loading state and this local minimum may be related to the level of tensile stress, σ_T, supported by the glass using the expression $\sigma_T \approx \frac{1}{2}\rho_o C_L \Delta u_{fs}$ (see e.g., Cochran, et al. 1977), where ρ_0 and C_L are, respectively, the initial glass density and longitudinal sound speed. For experiment S2G2, Δu_{fs} was 0.431 km/sec, which corresponds to a calculated value of σ_T = 35.9 Kbars. In cases where the glass fractures, σ_T is equal to the spall strength of the material.

The shock impedance of the aluminum impactor was comparable to that of the glass studied in these tests, so essentially full release of the glass from the impact state was possible through the initial right-going rarefaction if no spall occurred. Since the observed velocity history for S2G2 did show nearly full release, the σ_T value noted above (35.9 Kbars) may represent a lower bound on the spall strength of S-2 glass following shock compression to about 40 Kbars. This value is consistent with recently reported data (Wise, et al. 1992) that indicate σ_T = 33.5-34.9 Kbars for aluminosilicate glass following impact loading to 34-35 Kbars during experiments configured like those considered herein.

Experiments S2G1 and S2G3 also involved free-surface VISAR observations. However, the impact stresses for these tests (45 and 77 Kbars, respectively) were higher than that produced in shot S2G2. As a result, strong pullbacks in velocity like the one exhibited in experiment S2G2 were not obtained for S2G1 and S2G3. In shot S2G1, a slight decrease in free-surface velocity (Δu_{fs} = 0.014 km/sec) was discernible at t = 1.79 µsec (see Figure 3.1.2), corresponding to σ_T = 1.2 Kbar. For shot S2G3, no pullback was evident; instead, the arrival of a recompression was observed at t = 1.73 µsec (see Figure 3.1.4). These results suggest that the S-2 glass spalled during tests S2G1 and S2G3, and that the glass experiences a dramatic loss of spall strength for impact stresses exceeding about 40 Kbars when loaded in the present test configuration.

In view of the complex behavior displayed by the S-2 glass as described above, we chose to perform wavecode simulations of a portion of the experiments to get a more accurate description of the equation-of-state and spall behavior of the glass. This was done in an iterative fashion using CTH and varying the Hugoniot and spall parameters to achieve a "best fit" to the experimental velocity histories as measured for the lower impact conditions (i.e., those associated with the experiments S2G1-S2G3). As an example, Figure 3.1.12 demonstrates the accuracy of our fit to the data from experiment S2G2. The fitting procedure assumed a Mie-Grüneisen form for the equation-of-state of the glass. This, in turn, requires a knowledge of the Hugoniot curve for the glass. Through the fitting procedure, we have found that the dynamic behavior of the S-2 glass is best fit by the following U_S-U_P Hugoniot:

$$U_S = (4.4 + 1.6U_P)\ \text{km/sec},\ U_P \leq 0.5\ \text{km/sec}, \tag{3.1.1}$$

and by a spall strength of 37.57 Kbars, corresponding to a fracture strain of 0.056. Impact behavior above a particle velocity of 0.5 km/sec would require a separate description. However, this is not necessary for the conditions we wish to explore here. The dynamic behavior of S-2 glass, if needed, could be fitted for a broader range of particle velocities using a piecewise linear, or nonlinear U_S-U_P Hugoniot approximation.

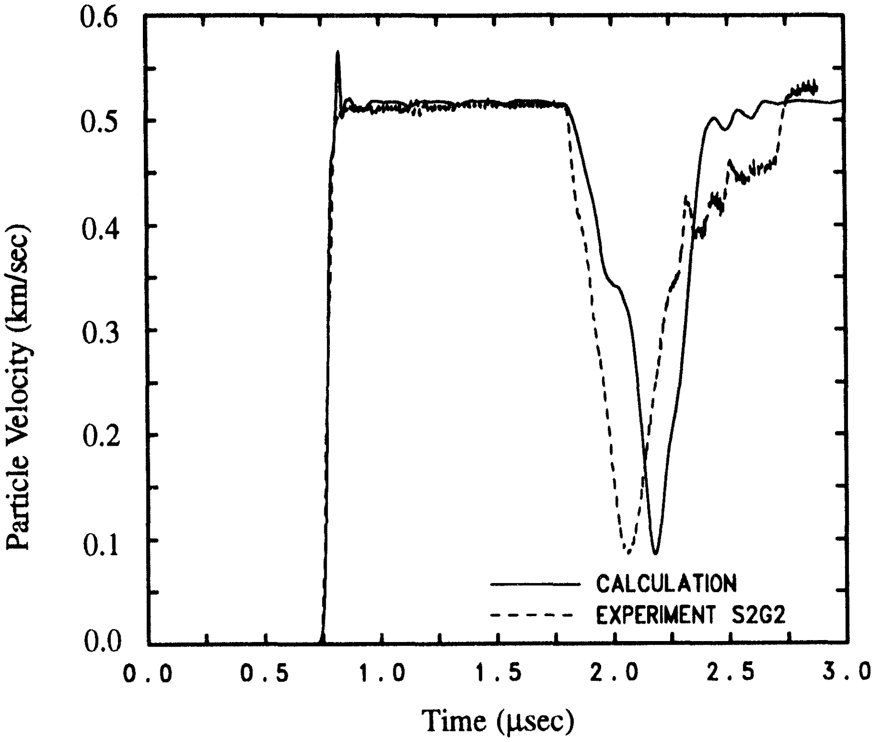

Figure 3.1.12. Comparison of "best fit" CTH simulation with experiment S2G2.

3.2 Epoxy Resin

3.2.1 Experimental Configuration

A series of six impact tests was conducted to characterize the Hugoniot and spall properties of the epoxy resin (UF-3283 adhesive) supplied by Thiokol Corporation. This resin is used as the matrix constituent of the S-2 glass/epoxy composite. These tests utilized the 100-mm compressed gas gun and the 89-mm powder gun at the Sandia STAR Facility.

The test matrix is presented in Table 3.2.1, with the basic experimental configuration illustrated in Figure 3.2.1. Tests EP-1, EP-2, and EP-3 successfully produced both Hugoniot and spall data, over a Hugoniot range of 5 - 27 Kbars. Tests EP-4 and EP-5 gave time-of-arrival (TOA) data, and hence Hugoniot data, but did not yield wave profiles. In the stress range of these experiments (56 to 105 Kbars), the epoxy free-surface apparently did not survive well enough to reflect the laser light necessary for velocity interferometry waveform measurements. Test EP-6 (145 Kbars) was conducted with a PMMA window to prevent similar surface breakup from occurring. As such, it affords Hugoniot and release properties of the resin, but not spall properties (there is no instance where multiple releases intersect within the sample). For this test, the observed wave was very nearly in-situ due to the close impedance match of the resin and the PMMA window.

Table 3.2.1: Gas and Powder Gun Test Matrix for Epoxy Resin

Shot No.	Impact Velocity (km/ sec)	Foam Thick. (mm)	Foam Density (g/cm^3)	Impact Mat. & Thick. (mm)	Sample Thick. (mm)	Sample Density (g/cm^3)	Window Mat. & Thick. (mm)	Vel. per Fringe (km/sec)
EP-1	0.197	8.021	0.454	Al 8.452	8.748	1.177	---	0.07167
EP-2	0.480	8.015	0.432	Al 7.498	8.749	1.177	---	0.07167
EP-3	0.841	8.025	0.424	Al 6.762	8.751	1.177	---	0.07167
EP-4	2.3096	5.038	0.633	Al 5.397	8.762	1.175	---	0.87264
EP-5	1.462	5.039	0.635	Al 5.982	8.760	1.176	---	0.87264
EP-6	2.283	5.051	0.633	Ta 2.775	8.7555	1.176	PMMA 26.182	0.45194

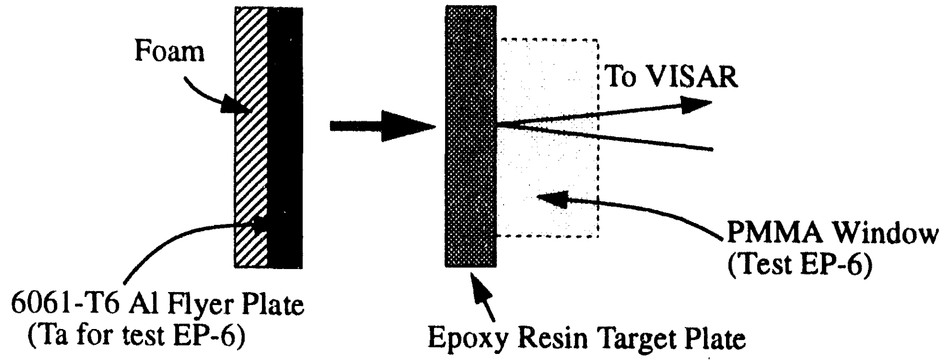

Figure 3.2.1. Schematic of geometry for Hugoniot/spall experiments on epoxy resin.

3.2.2 Particle-Velocity Measurements

Velocity profiles for the compressed-gas-gun tests are plotted in Figure 3.2.2. These tests

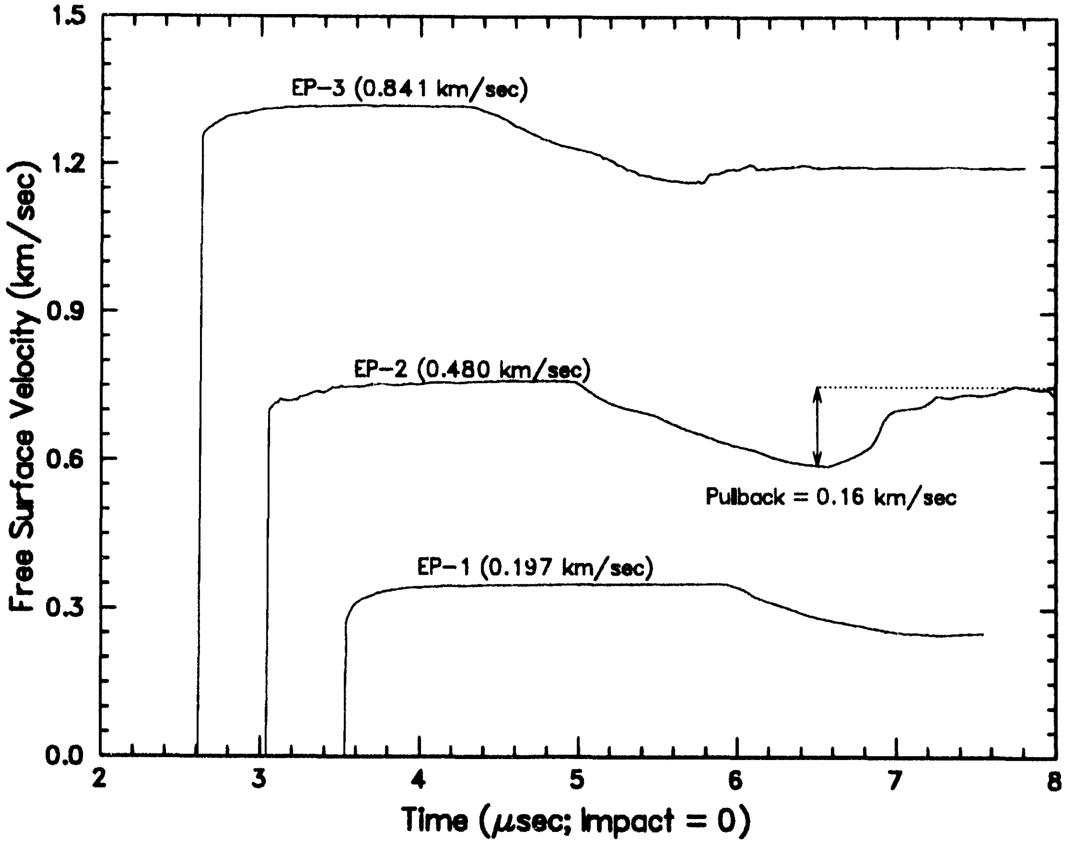

Figure 3.2.2. Velocity profiles for the compressed gas gun tests conducted on the UF-3283 epoxy resin. (See Table 3.2.1 for test parameters)

were conducted without windows (free-surface velocity monitoring) to give measurable spall signatures. As expected, the plateau levels in the three compressed-gas-gun tests are close to twice the in-situ Hugoniot particle velocity values, although there are deviations from this value. The ratio $U_{Plateau}/(2 \cdot U_{Particle})$ is 0.942, 1.033 and 1.013 for tests EP-1, EP-2 and EP-3, respectively. If the release of these samples had been precisely along the Hugoniot, these ratios would have been equal to 1.0. Deviations from unity suggest the occurrence of strength effects or irreversible compaction (probably the former). Hence, this effect is more pronounced in test EP-1 than in tests EP-2 and EP-3.

The timed velocity profile for EP-6, along with the times of arrival for the EP-4 and EP-5, are shown in Figure 3.2.3. The profile for test EP-6 cannot be directly compared to those of EP-1 through EP-3 because of the different configuration used in those tests.

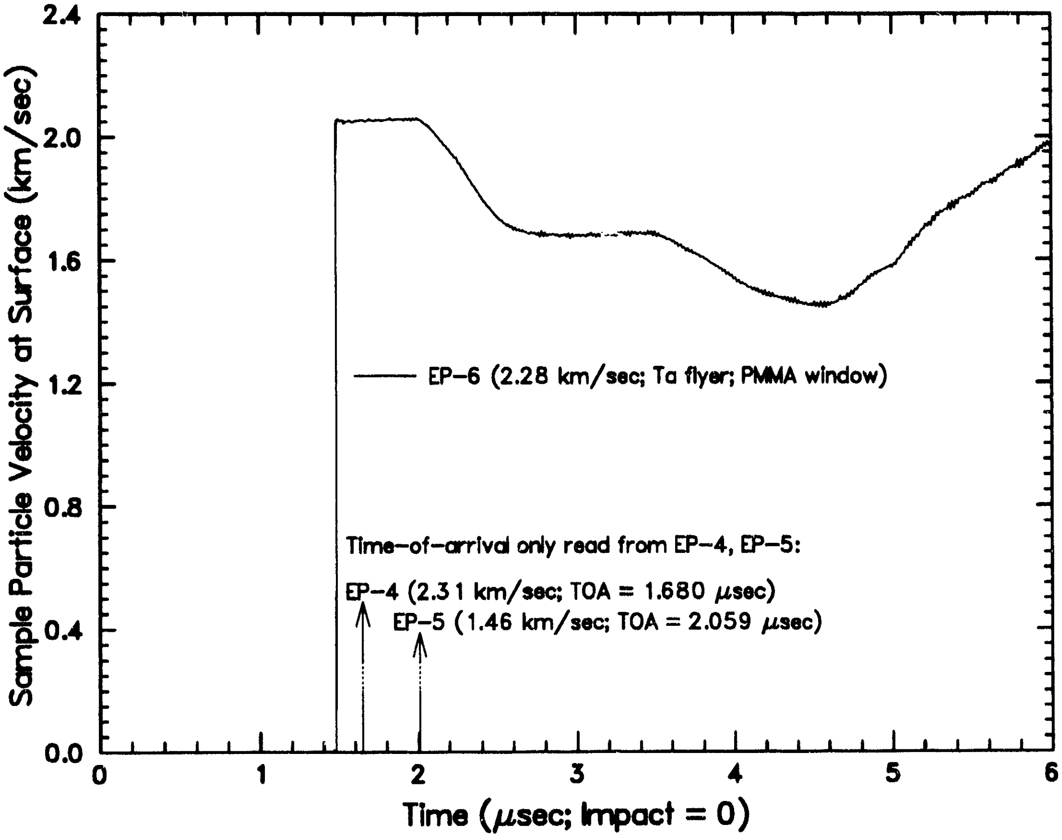

Figure 3.2.3. Velocity profile for powder gun test EP-6, and times-of-arrival for powder gun tests EP-4,5 conducted on the UF-3283 epoxy resin. (See Table 3.2.1 for test parameters)

The Hugoniot states for the epoxy resin are calculated by an impedance match in pressure/ particle-velocity space. This procedure is based on the assumption that while in contact, the impactor and target will experience the same interface pressure P and particle-velocity U_P. This state will lie at the intersection of the forward-going Hugoniot curve of the target, defined by the relation $P = \rho_0 U_S U_P$, and the backward-going Hugoniot of the impactor. The velocity of the shock wave in the sample, U_S, is calculated using time-of-arrival information with a knowledge of the target thickness. Thus, the determination of the Hugoniot state of the target relies on accurate timing of the waveform relative to impact along the center of the target, and on accurate measurement of the projectile velocity. The measured parameters from the experiments are presented in Table 3.2.2.

Table 3.2.2: Epoxy Resin Hugoniot and Spall Measurements

Shot No.	Impactor Material	Impactor Velocity (km/sec)	Initial Sample Density (g/cm^3)	Sample Thick. (mm)	Time-of-Arrival (μsec)	$U_{plateau}$ (km/sec)	Pullback Amplitude (km/sec)
1	Al	0.197	1.177	8.748	3.535	0.348	0.098
2	Al	0.480	1.177	8.749	3.048	0.755	0.165
3	Al	0.841	1.177	8.751	2.620	1.317	0.153
4	Al	2.3096	1.175	8.762	1.680	Not Meas.	Not Meas.
5	Al	1.462	1.176	8.760	2.059	Not Meas.	Not Meas.
6	Ta	2.283	1.176	8.755	1.481	Not Meas.	Not Meas.

3.2.3 Derived Hugoniot and Spall Properties of Epoxy Resin

The Hugoniot data for epoxy resin, determined from the data in Table 3.2.2, is presented in Table 3.2.3.

Table 3.2.3: Epoxy Resin Hugoniot Data

Shot Number	Particle Velocity, U_P (km/sec)	Shock Pressure, P (Kbars)	Shock Density, ρ (g/cm^3)	Shock Velocity, U_S (km/sec)	$\frac{\rho}{\rho_o}$
1	0.164	4.78	1.261	2.4747	1.0710
2	0.390	13.19	1.362	2.8704	1.1575
3	0.667	26.21	1.471	3.3401	1.2494
4	1.689	103.48	1.738	5.2155	1.4788
5	1.109	55.46	1.590	4.2545	1.3524
6	2.046	142.26	1.799	5.9115	1.5294

The Hugoniot properties of the epoxy (determined from the shock transit time, impactor material properties, and the projectile velocity) are similar to those of PMMA, although not identical. The epoxy Hugoniot is plotted in Figure 3.2.4 and compared with that of the window material, PMMA. The best fit to the shock-velocity/particle-velocity data of PMMA

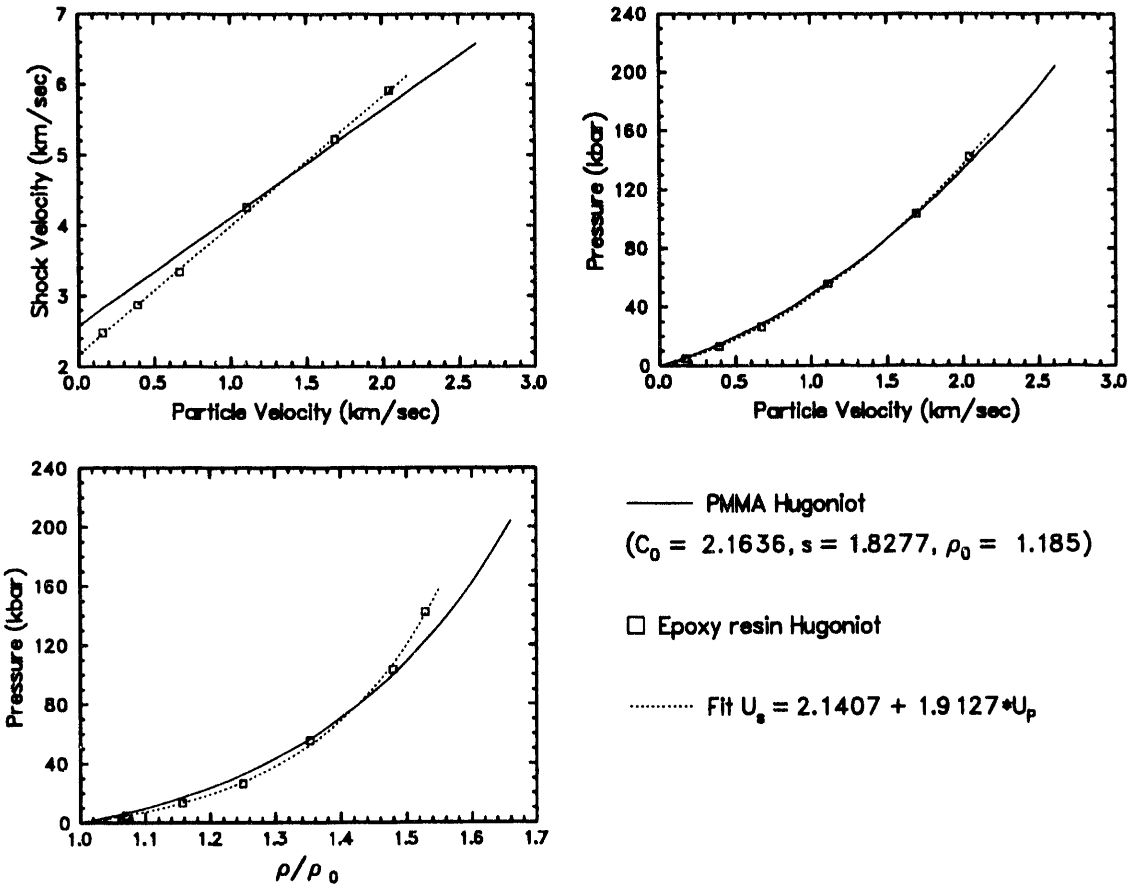

Figure 3.2.4. Measured Hugoniot of epoxy resin, compared with the Hugoniot of PMMA.

is represented by

$$U_s = (2.1636 + 1.8277U_p) \text{ km/sec.} \tag{3.2.1}$$

Fitting to the experimental Hugoniot data of the epoxy resin plotted in Figure 3.2.4 yields

$$U_s = (2.1407 + 1.9127U_p) \text{ km/sec.} \tag{3.2.2}$$

One-dimensional wave simulations of two of these tests have been conducted to obtain additional information. In particular, we performed simulations employing the wavecodes WONDY V (Kipp, et al. 1982) and CTH, assuming a simple Mie-Grüneisen model with adjustable spall strength for the epoxy resin.

In modeling test EP-2 using WONDY V, a spall strength of 2.5 Kbar roughly reproduced the observed pullback amplitude, while a strength of 3.0 Kbar prevented spall from occurring (see Figure 3.2.5). This suggests a spall strength of roughly 2.5 Kbar. Additional sim-

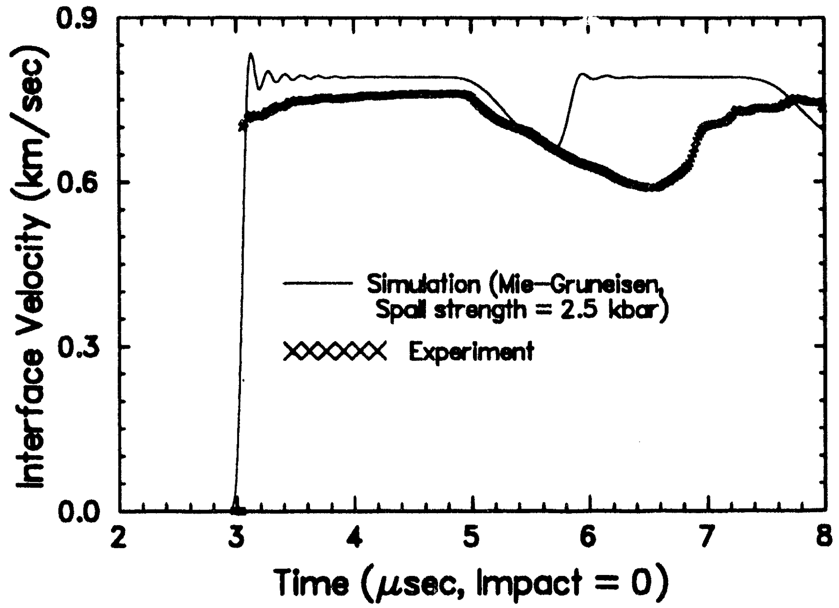

Figure 3.2.5. Test EP-2, showing observed and WONDY-generated wave profiles assuming a spall strength of 2.5 Kbars.

ulations employing CTH show that the experimental data is best fitted by a spall strength of 2.95 Kbars for the epoxy resin with a corresponding fracture strain of 0.0444.

The highest-pressure test (EP-6) was modeled to assess how closely a Mie-Grüneisen approximation, as the equation-of-state for the epoxy, would describe the behavior of this material. Since the PMMA window is a close impedance match for the epoxy resin, little wave perturbation was observed at the sample/window interface. This afforded an easy interpretation of the experimental results. In Figure 3.2.6, the WONDY-generated curve is overlaid on the experimental waveform. The arrival time and release profile agree well, with little disagreement at the plateau level. Hence the release of the material lies close to its Hugoniot curve, making the Mie-Grüneisen formulation an appropriate choice as equation-of-state for the epoxy material.

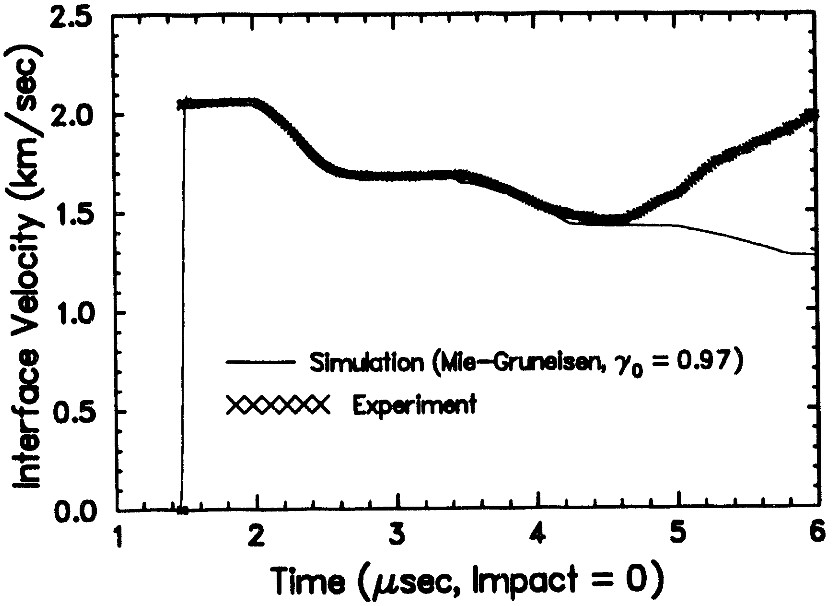

Figure 3.2.6. Test EP-6, showing observed and WONDY-generated wave profiles.

4. Description of Computer Codes to Model Composite Material Response

4.1 The CTH Code

The primary tool used in this study was the CTH code (McGlaun, et al. 1990). CTH is an Eulerian wavecode which is at present in wide use in the defense community in the United States. It is designed to model continuum mechanics problems involving large deformations at high rates, as would occur in strong shocks. Typical applications of CTH include armor/anti-armor problems and analysis of weapons performance and effects.

For the present study, CTH offers the advantage of an Eulerian framework. In this approach, the numerical mesh is fixed in space, while material is convected between the numerical cells. This is in contrast to the more common Lagrangian approach, in which the numerical mesh is tied to the material and deforms along with it. The Lagrangian approach has the disadvantage of sensitivity of the time step size to deformation of the material. Also, in regions of very large deformation, mesh tangling may occur in Lagrangian methods. Eulerian methods avoid these problems.

As an illustration of the advantages of the Eulerian approach for the simulation of composites, consider the case of two fibers initially separated by some thickness of matrix material (Figure 4.1). As the simulation progresses, the fibers eventually touch. If this problem were modeled with an Lagrangian code, the mesh representing the matrix material initially between the two fibers would have to be removed by some artificial means, because zero element widths are not permitted. This problem does not arise in an Eulerian code, because the mesh does not distort, and material flows between the cells. If further deformation occurs, voids might form due to material failure, and the Lagrangian code would again have difficulties due to the spontaneous creation of the voids in unpredictable

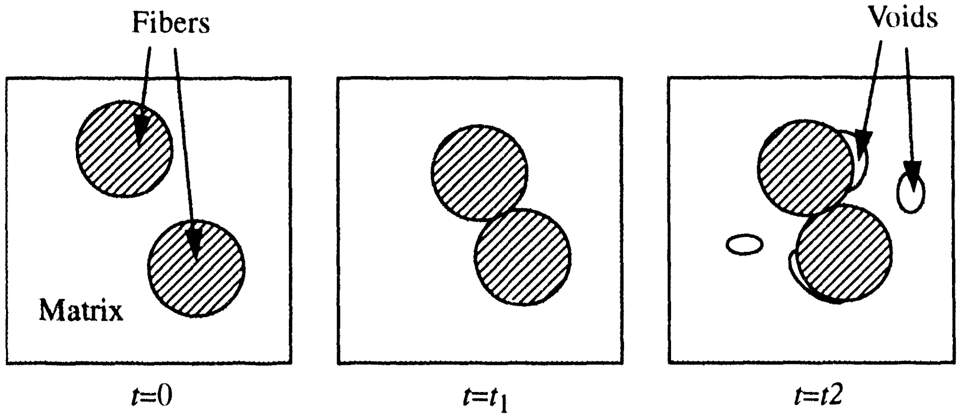

Figure 4.1. Illustration of phenomena that are difficult to model with a Lagrangian code: contact and void growth.

locations. Again, this problem does not arise in the Eulerian approach.

However, Eulerian methods also have disadvantages, notably an increase in requirements for numerical resolution, leading to an increase in cost over Lagrangian codes. Also, because Eulerian simulations inevitably involve mixed cells (numerical cells containing multiple materials or one material plus void), a range of troublesome issues arises concerning the treatment of the kinematic and physical properties of these mixed cells (Silling 1992; McGlaun 1991). For example, interfaces between materials in mixed cells are not precisely defined.

The issues regarding the treatment of mixed cells at fiber interfaces caused the most serious difficulties that arose in the application of CTH to composites simulation, and they were not entirely resolved. The principal problem was the tendency of fibers to stick to each other at points of contact. When two fibers touch within a numerical cell, they lose their identity for purposes of calculating the strength of the cell. Effectively, a tiny weld forms between the two fibers. This creates inaccuracy in modeling the sliding of fibers against each other.

4.2 Modifications to CTH

The CTH code was modified to allow two additional capabilities: prescription of deformation or loading histories, and computation of average material response within the composite. We now describe these modifications separately.

4.2.1 Prescription of Deformation or Load History

In simulations involving prescribed deformation at the boundary, we embed the numerical *sample* of composite within a region of separate material called the *frame* (Figure 4.2). The frame is composed of a fictitious material whose sole purpose is to cause the correct deformation history to be applied to the boundary of the sample. The mechanical and thermodynamic properties of the frame are irrelevant, since the entire motion of the frame is prescribed.

Why do we need the frame? Why can't the deformation history be applied directly to the boundary of the sample? The reason is that if the frame were not present, the boundary of the sample would, in general, occupy cells which are partially filled with void. The presence of void creates ambiguities and problems in attempting to prescribe a velocity within a cell. These ambiguities are related to the fact that a velocity assigned to void is meaningless. Therefore it is better to fill the exterior of the sample with some fictitious material (such as the frame) and prescribe velocities within this material.

Although the present report is not intended as a user's manual, it is perhaps of interest to show an example of how prescribed deformation histories are specified. The following is a typical example of input used to prescribe a deformation history. It would appear in the EPDATA input data set.

```
prescribed deformation
```

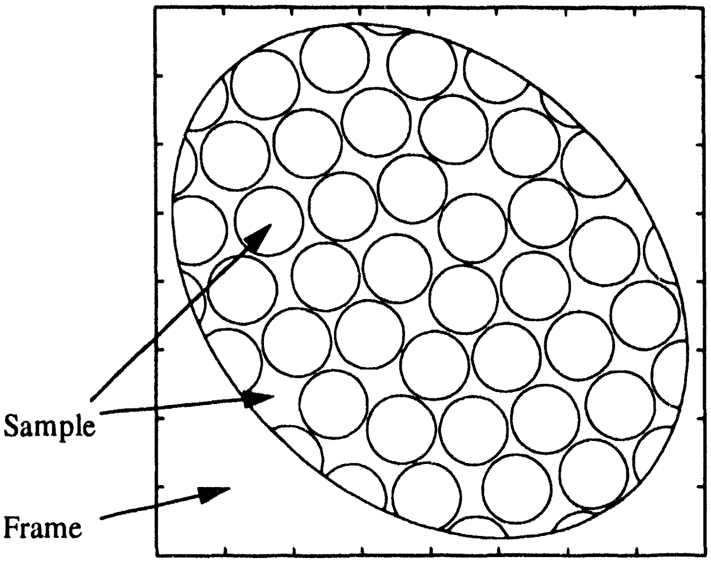

Figure 4.2. Composite sample surrounded by frame, to which a prescribed deformation is applied.

```
loadstep 1 begins_when time increases_thru 0
  rxx 1.0e5 rxy 0 ryx 0 ryy 1.0e5
loadstep 2 begins_when time increases_thru 50.0e-9
  rxx 0 rxy 0 ryx 0 ryy 0
loadstep 3 begins_when time increases_thru 100.0e-9
  rxx 0 rxy 2.0e5 ryx 0 ryy 0
loadstep 4 begins_when txy increases_thru 1.0e9
  stop
```

This input causes the sample to be subjected to the deformation history shown in Figure 4.3. The calculation stops when the average Cauchy stress component T_{xy} reaches the value 10^9 dyne/cm^2 (1 Kbar).

The current values of the components of the Eulerian velocity gradient tensor are computed in subroutine ELSG, based on the piecewise linear function specified in the user input. The actual application of the prescribed velocity gradient field occurs in subroutine ELVP, whose function is to integrate the velocity components at the cell faces based on the pressure gradient. (Deviatoric stress components are included separately, in subroutine ELVS.)

A prescribed load history is specified according to input similar to the following example. This input would appear in the EPDATA input set in CTHGEN:

```
prescribed stress
compliance 0.003
```

```
loadstep 1 begins_when time increases_thru 0
   qxx -1.0e17 qxy 0 qyy -1.0e17
loadstep 2 begins_when time increases_thru 50.0e-9
   qxx 0 qxy 1.0e16 qyy 0
loadstep 3 begins_when fxy increases_thru 0.1
   stop
```

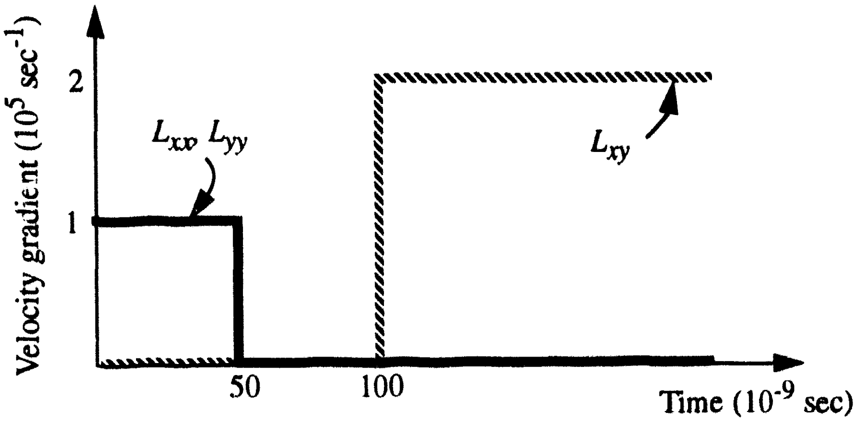

Figure 4.3. Deformation history supplied by the input shown in the text.

This input prescribes a piecewise linear loading history. The parameters `qxx`, `qxy`, and `qyy` are components of the Cauchy stress rate tensor $\dot{\mathbf{T}}$ (dyne-cm^{-2}-sec^{-1}). The `compliance` C is a number that is used to determine the current Eulerian velocity gradient tensor according to the following equation:

$$\mathbf{L} = C(\bar{\mathbf{T}} - \mathbf{T}_0), \qquad (4.2.1)$$

where $\mathbf{T}_0$ is the prescribed stress history and $\bar{\mathbf{T}}$ is current average stress in the window (see below). The components of **L** computed in this way are then applied to the frame as described above. Therefore Equation (4.2.1) provides a feedback mechanism by which changes in the stress in the composite are compared with the prescribed stress history, causing changes to be made in the deformation rate.

The input shown above would result in a stress history within the sample shown in Figure 4.4. The calculation stops when the deformation gradient tensor component F_{xy} reaches the value 0.1.

4.2.2 Computation of Averaged Variables within the Composite

To compute the bulk response of the composite represented by the sample, we can proceed

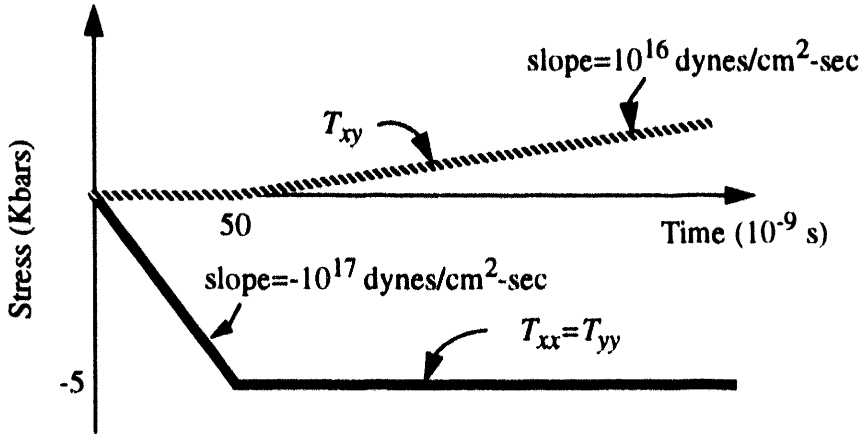

Figure 4.4. Stress history supplied by the input shown in the text.

in one of two ways: prescribe the deformation and find the average stress, or prescribe the stress and find the average deformation (in some sense). The means of prescribing either the deformation at the boundary or the stress were described in the previous section. In this section we discuss the means of computing the average response of the composite.

All averaging takes place within a subregion of the sample called the *window*. The window consists of all points in the sample at least a distance `rwin` from the boundary of the sample, where `rwin` is a user supplied number. The reason for not using the entire sample for averaging is that there are sometimes large edge effects near the boundary of the sample. For example, if the sample boundary passes through a fiber, the prescribed deformation at the boundary will result in excessive stress in the fiber, which is much stiffer and stronger than the composite as a whole. A typical window is shown as the shaded region in Figure 4.5. The window deforms along with the material at the microstructural level; i.e., a material particle initially in the window will remain in the window for the entire calculation. This is done to avoid influencing the averaged quantities merely through convection of one or another material into or out of the window.

The average Cauchy stress $\bar{\mathbf{T}}$ and average deformation gradient tensor $\bar{\mathbf{F}}$ in the window are computed in the straightforward way:

$$\bar{\mathbf{T}} = \frac{1}{V}\int_W \mathrm{T}\,dV, \qquad \bar{\mathbf{F}} = \frac{1}{V}\int_W \mathrm{F}\,dV, \tag{4.2.2}$$

where W denotes the window, which has volume V (a function of time), and **T** and **F** are the local Cauchy stress and deformation gradient tensors (functions of position and time). Several other average quantities are also computed, included fiber volume fraction, mass density, and volume fraction of failed material. The coding which performs the averaging is included in subroutine ELSG.

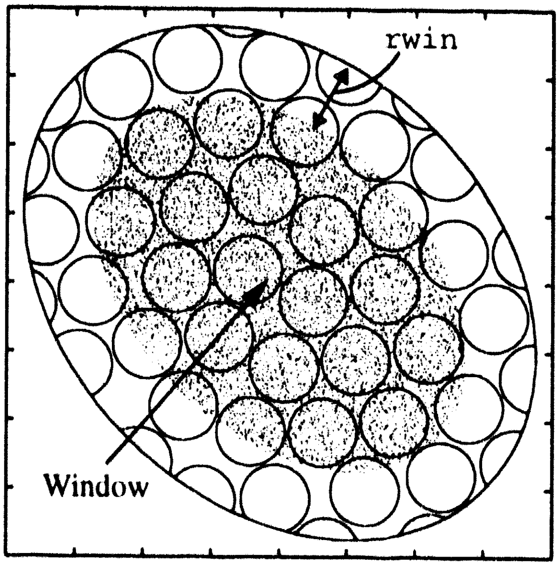

Figure 4.5. Averaging takes place within the window, a subregion of the sample.

At each time step, the average quantities are stored on a separate file called `mixhis.dat` for use by the post-processing program `history.f`. Upon restart, the existing `mixhis.dat` file, if one is present, is read. Only those values prior to the restart time are retained in the file. Thus the use of the file does not prevent the use of the standard CTH restart capability.

4.3 Assignment of Fiber Locations

Because there are typically many fibers in a calculation, it would be tedious to generate the CTHGEN material insertion packages for all the fibers by hand. Instead, we have written a preprocessing program called `relax.f` which generates the fiber locations and the corresponding CTHGEN input.

We assume that the fibers are distributed randomly in the sample. It is a simple matter to generate random coordinates for the fiber centers. The problem with this approach is that in general, the resulting fibers overlap. To prevent overlapping, we introduce a relaxation algorithm which causes the fiber centers to separate. This is done using a repulsive central force between the centers of any pair of fibers that overlap. Each "time step" causes the centers to move away from each other incrementally. (Note that we are dealing with only the fiber center coordinates, not the fibers themselves.) The relaxation process stops when no pair of fibers overlaps.

The final volume fraction of fibers after this relaxation process cannot be specified in advance. The only way to influence this volume fraction is to change the total number of fibers to be generated. This is easily changed by the user.

The `relax.f` program computes the final fiber volume fraction using an algorithm that makes use of a raster. Each dot in the raster is set to 0 or 1 depending on whether its location is occupied by matrix or fiber material. The total number of 1's divided by the total number of raster locations approximates the fiber volume fraction. The approximate volume fraction is printed on the screen, so the user can easily change the number of fibers if a different fiber volume fraction is desired.

The file `cth.i` is both the input and the output from the program. An existing `cth.i` file is left unchanged, except that the material insertion packages are changed to reflect the composite sample generated by the program. Thus the user rarely needs to change the material insertion packages directly.

4.4 Plotting of Averaged Variables

The averaged variables stored in the time history file `mixhis.dat` as described above are plotted with the help of the post-processing program `history.f`. This program reads the time history file and provides a menu displaying the variables contained in the file. Any combination of these may be plotted, or any variable may be plotted as a function of time. Multiple curves may be plotted on the same graph. Also, the results of multiple calculations may be plotted on the same graph. For each pair of variables plotted, the program generates a two-column ascii file containing the numerical values.

The post-processing program uses HISPLT, one of the graphics packages provided with CTH, as an x-y plotter. Many examples of plots of averaged variables are provided elsewhere in this report.

5. Numerical Experiments

5.1 Two-Dimensional Numerical Experiments

In this section, we describe the results of numerical experiments aimed at providing a strength/failure surface for unidirectional, fiber-reinforced plastic composites when deformations are restricted to planes perpendicular to the fiber direction. In this way, the influence of various microstructural features on the composite's mechanical response can be studied without the effects of material anisotropy coming into play.

In most applications of fiber-reinforced composites, structural strength and resistance to impact and penetration have been found, at least empirically, to depend on fiber volume fraction and the bonding strength between the constituents (i.e., reinforcement and matrix materials). Furthermore, during impact and penetration, the composite target experiences confining pressures anywhere in the range from 1 to 10 Kbars. In view of these observations, we have performed well-controlled numerical experiments that quantify the dynamic strength and failure characteristics of the S-2 glass/epoxy composite system subjected to various pressures, where the fiber volume fraction and the constituent bonding strength are varied within limits commonly found in the applications.

Our methodology consists of setting up a series of CTH simulations (referred to here as "numerical experiments") in which the glass volume fraction is varied between 60% and 73% and the constituent bonding strength is either perfect (equal to the volume-averaged strength of the constituents) or negligible. (In the jargon of composites, perfectly bonded materials are referred to as being "compatible," whereas negligibly bonded materials are "incompatible.") The material properties required in the calculations include only the equation-of-state and constitutive properties of the glass and epoxy constituents. That is, *no composite properties are required.* The constituents were modeled with the Mie-Gruneisen equation of state using Hugoniot and fracture properties reported in section 3. The constitutive properties were determined using ultrasonic wave-speed measurements and split-Hopkinson bar experiments (Olsson 1993). The deviatoric response of each constituent is modeled as elastic-perfectly plastic. All material properties data required by the calculations appear in Table 5.1.1.

Table 5.1.1: Constituent Material Properties for Microscale Simulations

Material Property	Epoxy	S-2 Glass
Density (g/cm^3)	1.177	2.492
Linear U_s-U_p Hugoniot Y-Intercept (cm/sec)	2.141×10^5	4.40×10^5
Linear U_s-U_p Hugoniot Slope	1.913	1.60

Table 5.1.1: Constituent Material Properties for Microscale Simulations

Material Property	Epoxy	S-2 Glass
Gruneisen Parameter	1.130	0.90
Specific Heat, C_v (erg/g-eV)	1.253×10^{11}	0.855×10^{11}
Poisson's Ratio	0.359	0.238
Yield Strength (Kbars)	1.70	46.9
Uniaxial Fracture Strain	0.0444	0.0560

We have conducted a series of numerical experiments that explore the dependencies of the material response on both the microstructure and the constraint of confining pressure. The initial setup of the sample to a specific fiber volume fraction has already been described in section 4 and illustrated in Figure 4.2. After initial setup, we impose a pressure-stress history on the composite sample by starting with isotropic contraction or expansion of the frame, at a constant rate of 10^{17} dynes/cm^2-sec, to a particular value of pressure. These pressures were nominally -1, 0, 5, and 10 Kbars. Following the compression, and holding the pressure fixed, the samples were then subjected to identical shear stresses that are increased linearly with time at the rate of 10^{16} dynes/cm^2-sec. These loading histories are shown schematically in Figure 5.1.1. As a result of this loading history, the composite sample typically experiences strain rates ranging from 10^5 to 10^6 sec^{-1} at the point of failure. Since our interest lies with the investigation of microstructural influences under impact conditions, we have not looked at rate dependencies of composite response beyond subjecting the material to the range of strain rates typically associated with impact.

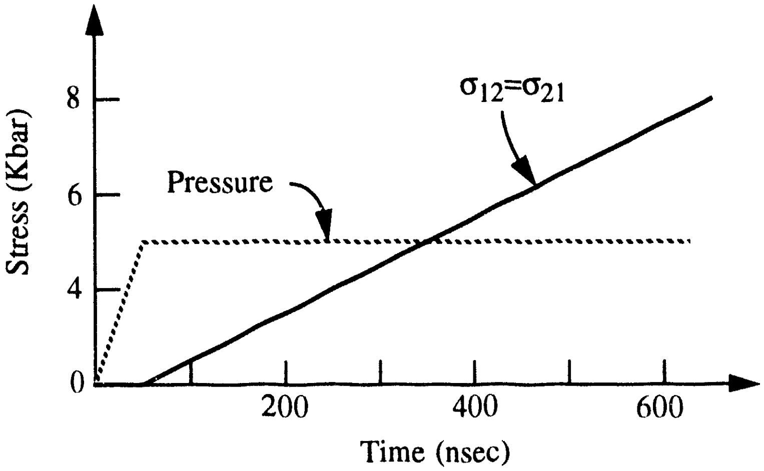

Figure 5.1.1. Pressure-shear loading history schematic.

We performed this sequence of simulations at two different initial fiber volume fractions, 60.1% and 72.8%, both possessing perfect constituent bonding. Additional calculations were conducted for an initial fiber volume fraction of 72.8% with perfect and negligible constituent bonding. The results of these numerical experiments are represented by the shear stress vs. shear strain plots at various confining pressures appearing in Figures 5.1.2 through 5.1.6. Figure 5.1.2 illustrates the pressure-shear response of a composite at 72.8% fiber volume fraction and perfect constituent bonding.

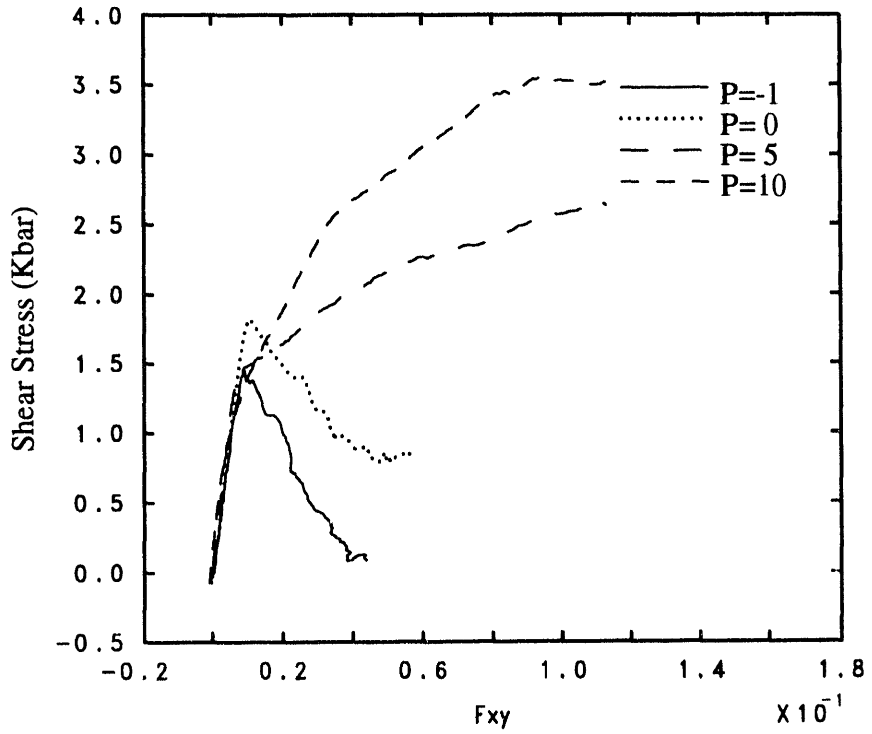

Figure 5.1.2. Shear stress vs. shear strain for various pressures at 72.8% fiber volume fraction and perfect constituent bonding.

Note the monotonic increase in failure stress as a function of confining pressure. In this figure, two distinct mechanisms of failure are displayed by the composite. At the lower pressures of -1 Kbar and zero, failure is controlled by fracture and void growth in the epoxy matrix. In these cases, the glass fibers remain sufficiently separated such that they act as rigid, noninteracting inclusions embedded in a deformable epoxy matrix. Figure 5.1.3 illustrates the post-failure state of the composite initially subjected to zero pressure. Note the presence of voids in the matrix and lack of contact between the glass fibers. At the higher pressures (5 and 10 Kbars), the composite is compressed to the point where the response of the composite is dominated by the interactions of the glass fibers. That is, the epoxy matrix is distorted to the point that the glass fibers are in contact and, with further shear deformation, begin to slide past each other in a process we refer to as "fiber slip." Yield/failure in these instances is associated with the asymptotic flow behavior of a granular-like material. The post-yield/failure state of the composite subjected to an initial pressure of 10 Kbars appears in Figure 5.1.4. Note the absence of voids in the matrix and the contact between the glass fibers.

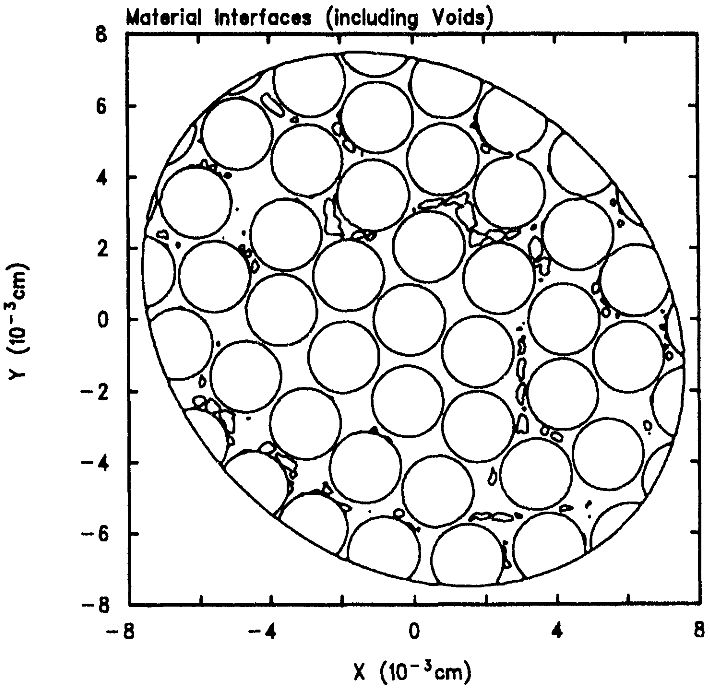

Figure 5.1.3. Post-failure state of perfectly bonded composite (72.8% fiber volume fraction) initially at zero pressure.

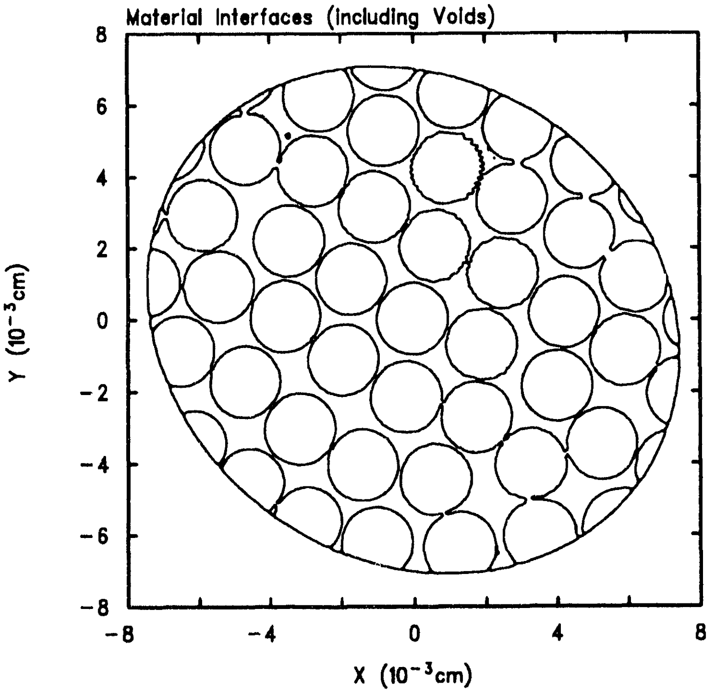

Figure 5.1.4. Post-failure state of perfectly bonded composite (72.8% fiber volume fraction) initially at 10 Kbars pressure.

Figure 5.1.5 depicts the response of a composite at the same initial fiber volume fraction of 72.8% but with negligible bonding strength between the constituents.

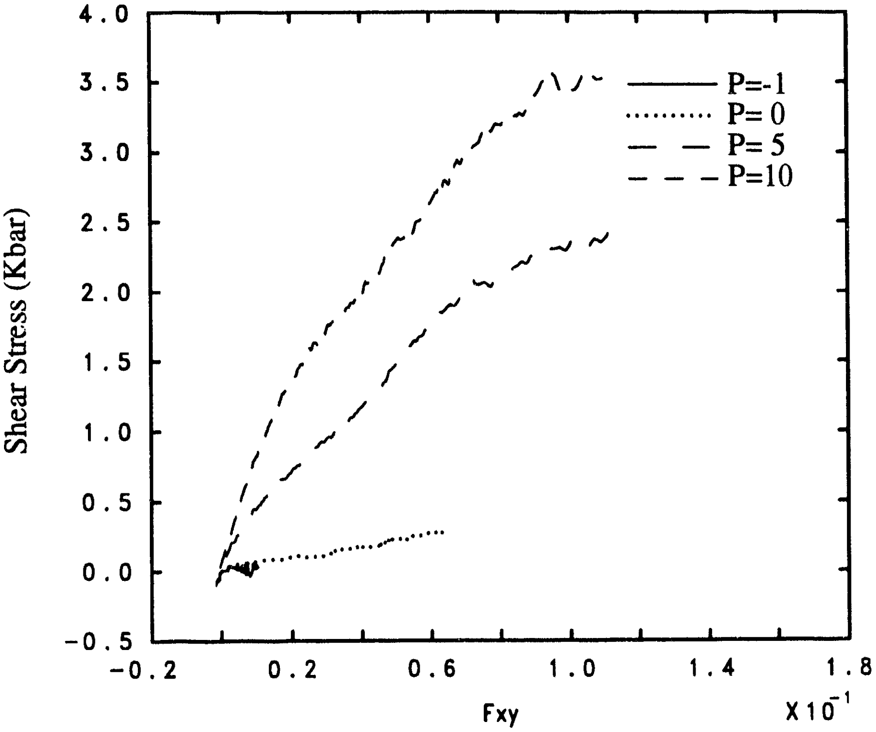

Figure 5.1.5. Shear stress vs. shear strain for various pressures at 72.8% fiber volume fraction and negligible constituent bonding.

Here again, the failure stress increases monotonically with pressure. Note the reduction in failure stress at the lower pressures when compared to the perfectly bonded case in Figure 5.1.2. Also, as with the previous case, the negligibly bonded material's failure is dominated by matrix fracture and void growth at the lower pressures and fiber contact with slip at the higher pressures. At the higher pressures, however, the negligible-bond case approaches that of the perfect-bond composite behavior.

Figure 5.1.6 depicts the response of a composite possessing an initial fiber volume fraction of 60.1% with perfectly bonded constituents. Note the inverse dependence of the failure stress on the pressure amplitude (i.e., failure stress decreases as pressure amplitude increases). Thus, at the initial fiber volume fraction of 60%, the failure behavior of this composite is dominated exclusively by the failure response of the matrix. The results of these particular simulations predict that, during the application of pressure before the shear deformation, the matrix suffers an amount of damage that is monotonically dependent on the final pressure amplitude. This damage is then compounded by the ensuing shear deformation. Without the mechanism of fiber contact and slippage to supplant this failure process, the resulting composite behavior is restricted to the peculiar response depicted in Figure 5.1.6. The decrease in failure stress for 1 Kbar of tensile pressure relative to the zero pressure case, suggests that the same failure mechanism is operating for tensile as well as com-

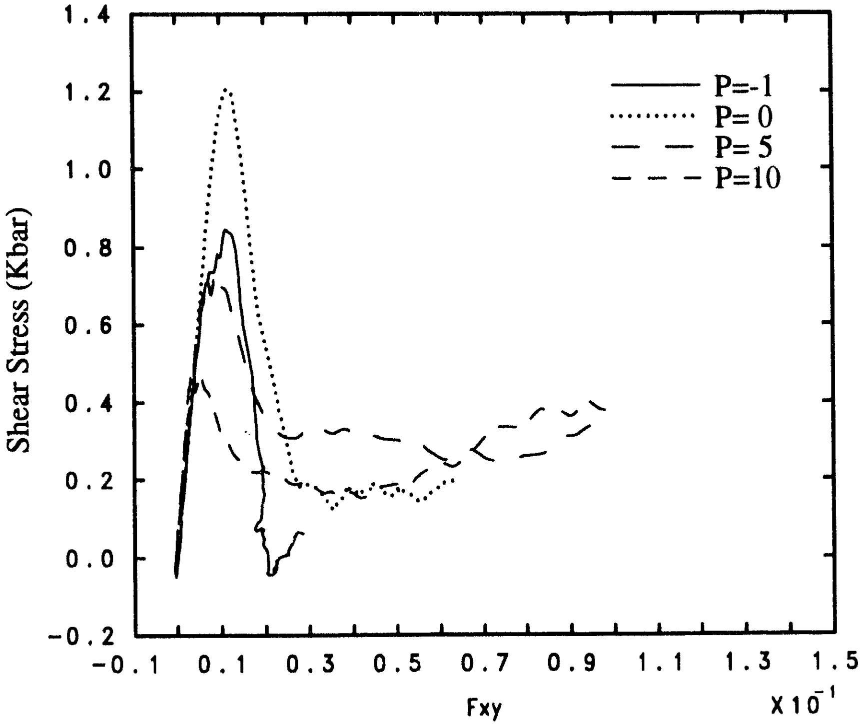

Figure 5.1.6. Shear stress vs. shear strain for various pressures at 60.1% fiber volume fraction and perfect constituent bonding.

pressive pressures.

The data appearing in Figures 5.1.2-5.1.6 clearly demonstrates the dependence of the composite's behavior on pressure. In fact, the yield/failure behavior of the composite in the planes normal to its reinforcement displays both cohesive and frictional behaviors. Cohesive behavior is typical of the constitutive response of metals which are pressure insensitive, whereas frictional behavior is representative of soils which display a dependence on pressure. This failure behavior can be represented by the following relation (Nelson 1977):

$$\sqrt{J_2} = f(P), \tag{5.1.1}$$

where $J_2 = \frac{1}{2} S_{ij} S_{ij}$ is the second invariant of the deviatoric stress tensor **S** and f(P) is a function of pressure that is fitted to the composite's constitutive response as represented in Figures 5.1.2-5.1.6. Under the existing conditions of plane-strain and the applied stresses of the pressure-shear calculations, J_2 becomes

$$J_2 = \frac{1}{3} (\sigma_1^2 + \sigma_2^2 + \sigma_3^2 - \sigma_1\sigma_2 - \sigma_2\sigma_3 - \sigma_3\sigma_1) + \tau_{12}^2, \tag{5.1.2}$$

where σ_1, σ_2, and τ_{12} are the nonzero normal and shear stresses in the plane perpendicular to fiber direction and σ_3 is the normal stress along the fiber direction. (The constraint of plane strain forces σ_3 to be nonzero.) Plotting the results of the numerical experiments in P-$\sqrt{J_2}$ space, we can demonstrate the construction of failure surfaces which can be analytically represented by eq.(5.1.1) as well as to illustrate the influence of the microstructural aspects of the composite.

Figure 5.1.7 represents the influence of constituent bonding on the failure surface of a composite at 72.8% initial fiber volume fraction.

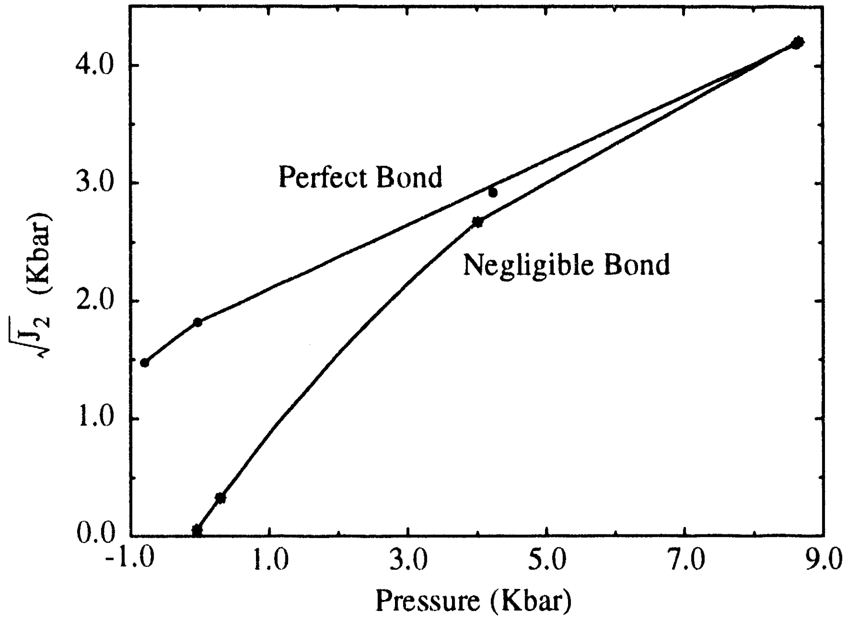

Figure 5.1.7. Failure surfaces for 72.8% fiber volume fraction with perfect and negligible constituent bonding.

At low pressures, the influence of the bonding is significant with the perfectly bonded material substantially stronger. However, this distinction disappears as the confining pressure increases.

The effects of varying the initial fiber volume fraction are depicted in Figure 5.1.8 where the failure surfaces of a perfectly bonded composite at 60.1% and 72.8% are compared. The most conspicuous result illustrated in Figure 5.1.8 is the marked increase in failure strength as the initial fiber volume fraction is increased from 60% to 73%. The almost linear response of the 73% composite while under compressive pressures is illustrative of a failure model proposed by Drucker and Prager (1952) for granular materials in which the function f(P) in eq.(5.1.1) assumes a linear form. The response of the 60% composite consists of both pressure-independent and dependent regimes. That is, at pressures between zero and 4 Kbars, the composite's behavior is dominated by the response of the epoxy matrix (whose constitutive response was modeled by von Mises plasticity which is pressure insensitive). As the confining pressure is increased, the epoxy matrix is distorted to the point that the glass fibers are brought into contact, thereby permitting fiber slip to occur

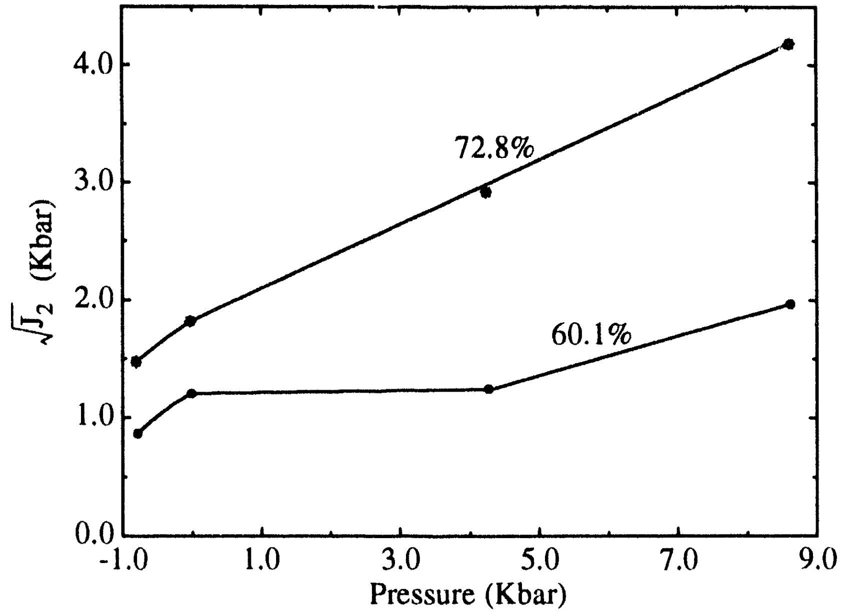

Figure 5.1.8. Failure surfaces for perfectly bonded composites at 60.1% and 72.8% fiber volume fraction.

with the ensuing application of shear stress. The process of fiber slip causes the composite to behave like a frictional material, displaying pressure-dependent yield/failure. This behavior suggests the existence of a critical fiber volume fraction at which the composite exhibits a transition from a cohesive material (pressure-independent) to a frictional material (pressure-dependent). Furthermore, our studies suggest that the critical fiber volume fraction occurs at the point for which the reinforcing constituent (glass) begins to interact with itself.

Various empirical studies (Bless, et al. 1985; Vasudev, et al. 1987) on glass fiber-reinforced composites have reported that composites with incompatible bonding (i.e., negligible constituent bonding) display superior ballistic performance over the same materials with compatible (perfect) bonding. The following two figures compare the effects of constituent bonding on a 72.8% fiber volume fraction composite at 10 Kbar confining pressure. In Figure 5.1.9, one can see that the shear stress-shear strain responses of the two materials are practically identical. However, a plot of the corresponding volume fractions of failed matrix material (i.e., epoxy material that has exceeded its failure strain as listed in Table 5.1.1), presented in Figure 5.1.10, shows a significant difference in the amount of damage sustained in the two cases. The composite with perfect bonding strength has sustained a significant amount of damage; i.e., by the conclusion of the experiment, almost all of the matrix material has failed (exceeded its failure strain). In the case of the composite with negligible bonding strength, very little of the matrix has failed. This result suggests that the perfectly bonded composite would, upon reloading, behave as a frictional material without any cohesive properties, similar to a dry granular material whose ability to support shear loads is highly dependent upon a confining pressure. The negligibly bonded materi-

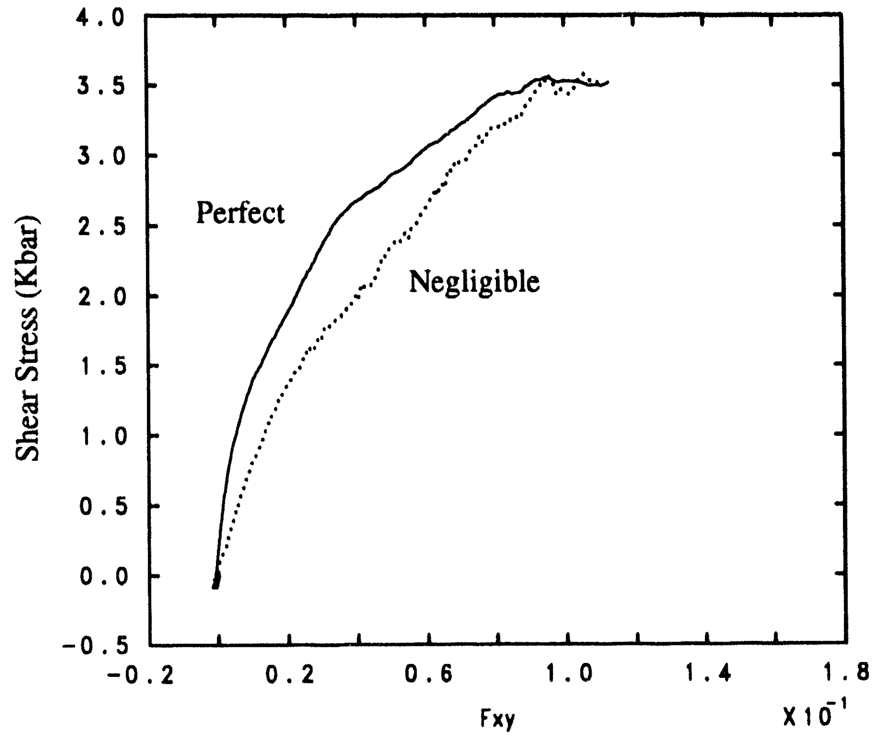

Figure 5.1.9. Shear stress vs. shear strain for perfect and negligible bonding. Composite at 10 Kbars pressure with 72.8% initial fiber volume fraction.

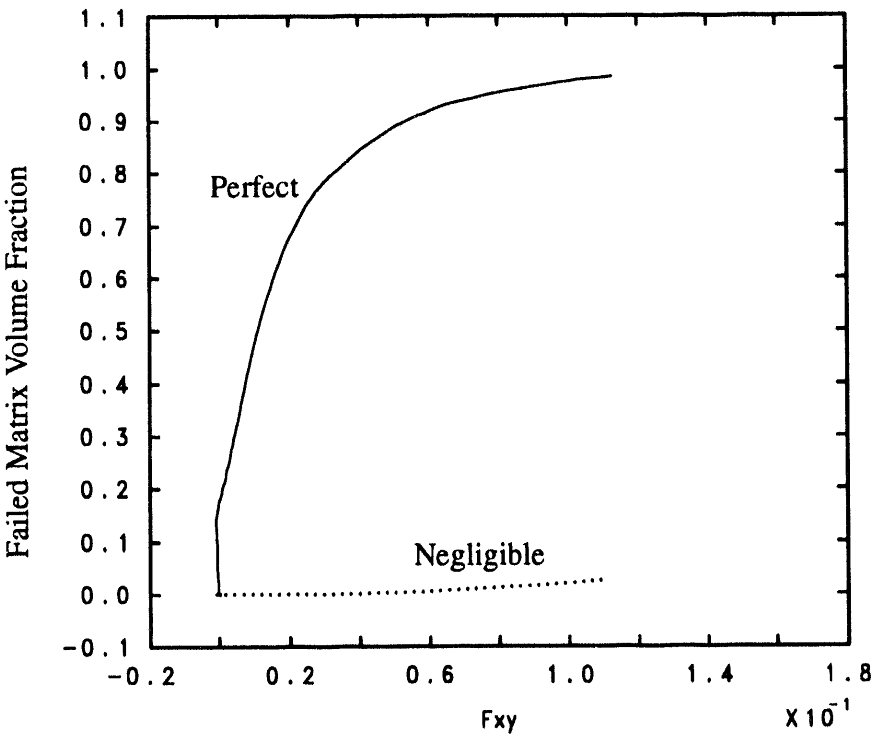

Figure 5.1.10. Failed matrix volume fraction vs. shear strain for perfect and negligible bonding. Composite at 10 Kbars pressure with 72.8% initial volume fraction.

al, however, would retain its cohesive properties upon reloading, thereby maintaining its ability to support loads that are not necessarily accompanied by a confining pressure for a greater period of time during the loading history of the material.

Thus, negligible bonding between the constituents causes impact-induced damage to accumulate at a rate significantly less than that which occurs for the perfectly bonded case. These results are consistent with the ballistic studies on glass-reinforced plastics, previously mentioned, where failure is delayed in the incompatible (negligibly bonded) material relative to the compatible (perfectly bonded) material. As a result, incompatible composite materials display a superior ability to resist penetration of a ballistic projectile than do the compatible materials.

5.2 Three-Dimensional Numerical Experiments

In this section we present a demonstration of the three-dimensional microscale modeling techniques for composites that were developed for this project. The original goal had been to use these techniques to derive a failure surface for an anisotropic composite, and to compare this prediction with experimental data on a real material. However, time and funding limitations did not permit this goal to be achieved. Nevertheless, the modeling techniques are in place, and they are readily applicable to this purpose.

We consider the response of a unidirectional glass/epoxy composite similar to that discussed in the previous section. The CTH model of a sample of this material is shown in Figure 5.2.1. The length of the sample in the z-direction is more than twice the length in the x- and y-directions because large end-effects occur in the calculations. For example, when the ends of the fibers are subjected to prescribed deformations, large stresses occur within the fibers. These stresses die away only gradually as one moves toward the interior of the sample. Therefore a long sample is required so that the overall state of stress near the center will more accurately reflect what would occur in a much larger composite body as it deforms. For the same reason, the window in the three-dimensional case was taken to be a sphere centered at the center of the sample, intentionally omitting the regions near the ends of the fibers.

It is apparent from Figure 5.2.1 that fewer fibers were included in the three-dimensional numerical sample than in the two-dimensional samples discussed previously. This was due to the practical requirement for a coarser mesh in three dimensions, because of the high cost of finely zoned three dimensional calculations. Each fiber diameter in the three dimensional calculations occupied about 10 cell widths, compared with 16 in the two-dimensional case. Because of this sacrifice in resolution, it was necessary to cut down the number of fibers. Also, because of this loss of resolution, the numerical problems that arise near sliding surfaces between fibers are aggravated in three dimensions. (See Section 4.2.)

As an illustration of the use of the three-dimensional modeling technique to predict anisotropic response in composites, we subject the sample to a pressure increase of 5.0 Kbars followed by simultaneously increasing shear stress components σ_{xy} and σ_{zx}, as shown in

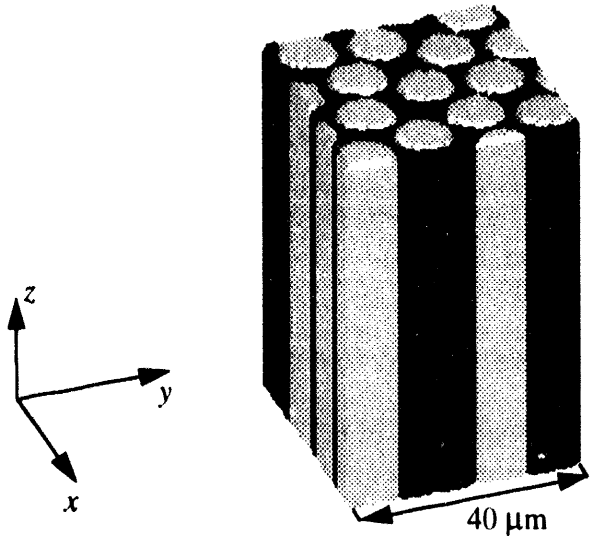

Figure 5.2.1. Three-dimensional model of a numerical sample of unidirectional reinforced composite.

Figure 5.2.2.

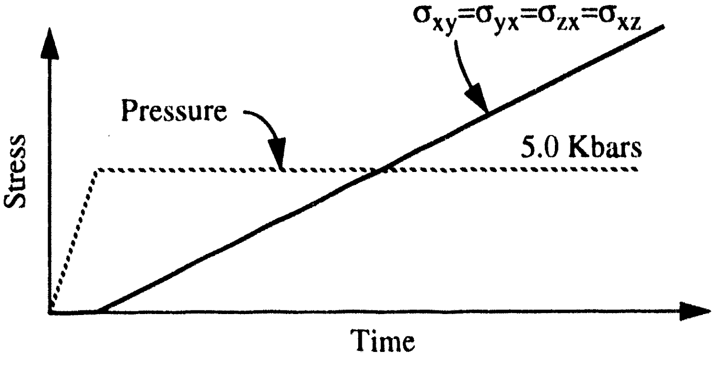

Figure 5.2.2. Pressure-shear loading history schematic.

The material properties and loading rates in this simulation were identical to those used in the two-dimensional calculations discussed in the previous section.

To help characterize the macroscopic failure properties of the composite undergoing this loading history, we use the histories of the stress components σ_{xy} and σ_{zx} (Figure 5.2.3). The figure shows that both these components attain maxima. However, we assume that failure occurs at the earlier of these maxima, which is t^*=250 nsec. At this time, the stress

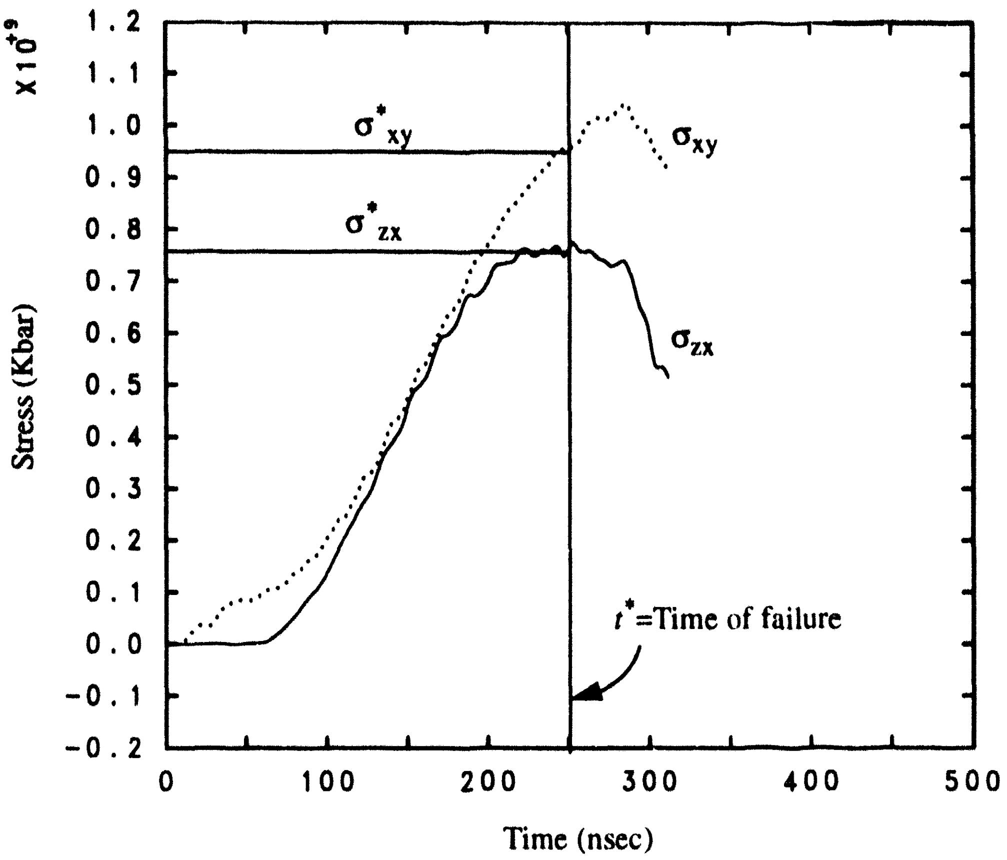

Figure 5.2.3. Time history of stress components σ_{xy} and σ_{zx}.

components are σ^*_{xy}=0.96 Kbar and σ^*_{zx} =0.77 Kbar. The former of these is larger because interactions between fibers stiffen the material against shear deformation within the cross-sectional plane, but not in other planes.

Note that the stress components shown in Figure 5.2.3 diverge as the failure approaches, while the applied loading history shown in Figure 5.2.2 does not reflect this divergence. The reason for this difference is that as the material starts to fail, it becomes impossible to accurately control the stress components. Eventually, the stress components reach maxima and then decrease upon further loading.

To characterize the state of straining that occurs as the material fails, we consult the histories of the Eulerian velocity gradient tensor components L_{xy} and L_{zx} (Figure 5.2.4). To be consistent with the usual terminology, we identify these with the "strain rate" components $\dot{\varepsilon}_{xy}$ and $\dot{\varepsilon}_{zx}$. At the time of failure, t^*, these strain rate components are $\dot{\varepsilon}^*_{xy}$=9.2x10^4 sec^{-1} and $\dot{\varepsilon}^*_{zx}$=10.2x10^4 sec^{-1}.

Using these results, together with the results of similar computations for the cases of non-

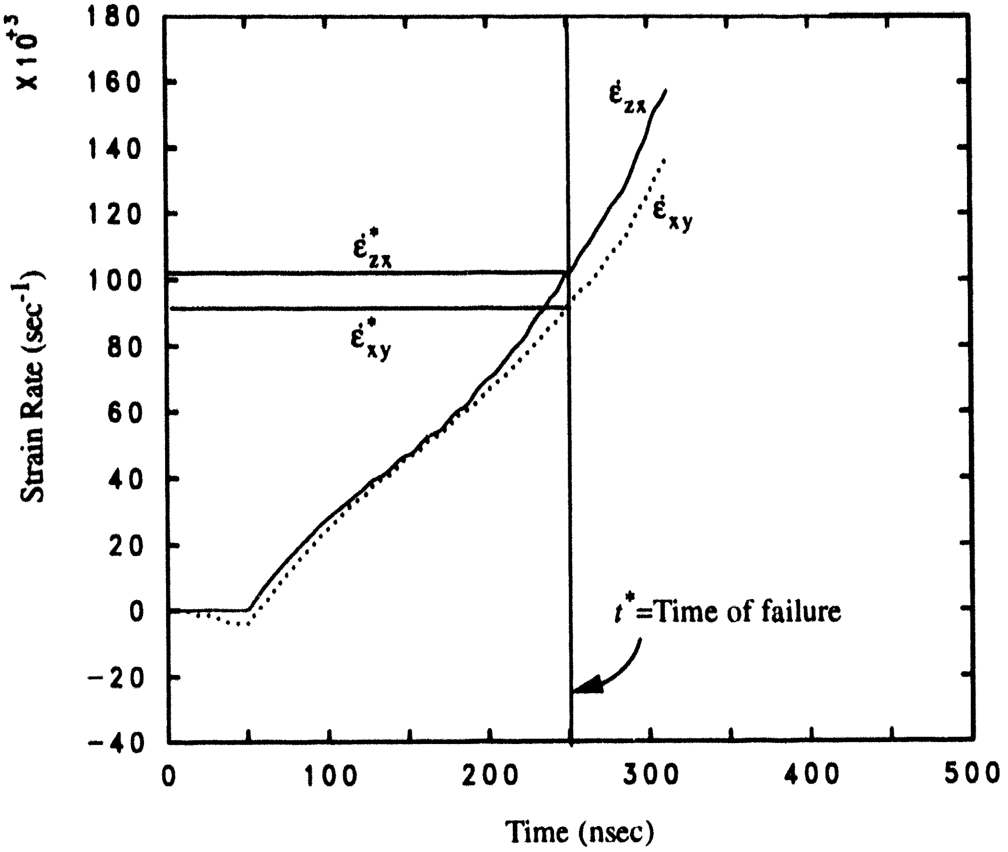

Figure 5.2.4. Time history of strain rate components $\dot{\varepsilon}_{xy}$ and $\dot{\varepsilon}_{zx}$.

zero σ_{xy} only and nonzero σ_{zx} only, we can construct a crude approximation of the cross-section of the failure surface of the composite in the σ_{xy}-σ_{zx} plane (Figure 5.2.5). This failure surface applies only to the value of hydrostatic pressure under consideration, 5.0 Kbars. The figure also shows the direction "vectors" corresponding to the strain rates at failure found from the calculations. The failure surface shown in the figure was constructed under the assumption of normality. This assumption could be checked by carrying out more calculations for other loading histories, populating the yield surface more densely.

The failure surface shown in Figure 5.2.5 reflects the anisotropic nature of the material response. There are certainly other possible loading histories which would show more prominent anisotropy, for example uniaxial tension in various orientations relative to the fiber directions. This type of loading path is easily applied in an experiment. However, the present example of compression followed by shear demonstrates the usefulness of the numerical microscale modeling approach in exploring some of the subtleties of anisotropic response in loading paths which would be difficult to produce experimentally.

The results presented in this section demonstrate the usefulness of three-dimensional micromechanical modeling in gaining an insight into the deformation and failure of compos-

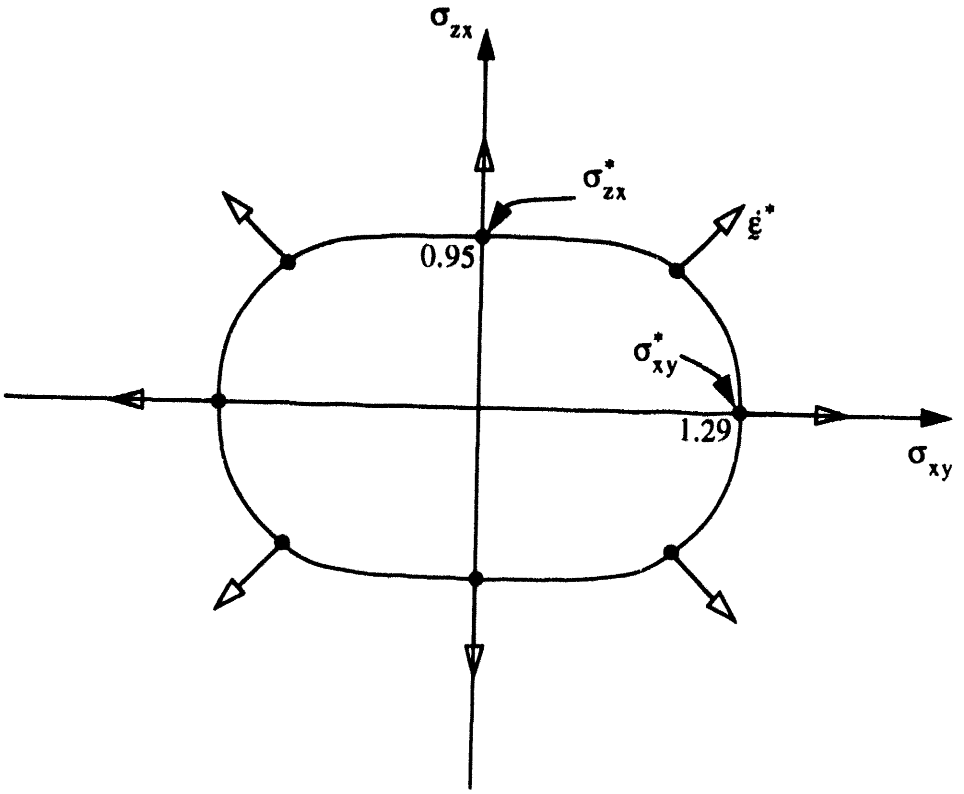

Figure 5.2.5. Failure surface constructed from calculated results.

ites, and in constructing failure surfaces. At present, the laborious and costly nature of large three-dimensional calculations restricts the number of data points that may be used to construct failure surfaces. A proper derivation of a failure surface would require many calculations. Nevertheless, computer hardware is improving rapidly, particularly in the area of massively parallel machines, and the next generation of computers should allow accurate prediction of three-dimensional failure surfaces to become more routine.

6. Summary

In this report, we have described a methodology that permits the modeling of complex mechanical behavior of heterogeneous materials based solely on a knowledge of the material's composition and microstructural morphology. We have applied this methodology to advance our understanding of a particular glass/epoxy composite material of interest to the aerospace and defense communities. In order to do so, we have performed the initial experimental research leading to the determination of equation-of-state and constitutive properties for the composite's constituents, namely, Owens-Corning S-2 glass and Thiokol epoxy resin (UF-3283).

In order to carry out microscale simulations, we developed the computer software needed to perform, and analyze, numerical experiments leading to an understanding of the dynamic response of a class of composite materials in both two and three dimensions. Using this approach, we are able to circumvent protracted experimental efforts to determine the influence of various microstructural aspects on a composite's behavior. Instead, further experimental work can concentrate on creating a database for validation of the constitutive models that are determined with the aid of microscale simulation.

The methodology of conducting numerical experiments that lead to the development of constitutive models for advanced materials is in its infancy. Although additional work for validation is still necessary, we believe this approach has the potential to assist engineers in the development of advanced materials designed for specific applications. One could envision, for instance, embedding software modules, similar to those we have developed for this project, into an algorithm that designs a composite whose properties have been optimized for a particular application.

Further work, on our part, will focus on obtaining and using experimental data to validate the microscale simulations on glass/epoxy and glass/polyester composites. These results may be used in the development of anisotropic constitutive models for glass reinforced plastics (GRP's) to be implemented in wavecodes such as CTH. Additional work will focus on the microscale simulation and constitutive model development for other materials such as carbon fiber composites and reinforced concrete.

References

L. M. Barker and R. E. Hollenbach, 1972, "Laser Interferometer for Measuring High Velocities of Any Reflecting Surface," J. Appl. Phys. **43**, pp. 4669-4675.

S. J. Bless, D. Hartman, and S. J. Hanchak, 1985, "Ballistic Performance of Thick S-2 Glass Composites," in *Symposium on Composite Materials in Armament Applications*, UDR-TR-85-88A.

L. C. Chhabildas and D. E. Grady, 1983, "Shock Loading Behavior of Fused Quartz," in: *Shock Waves in Condensed Matter*, edited by J. R. Asay, R. A. Graham, and G. K. Straub (Elsevier Science Publishers B.V., New York, 1984), pp. 175-178.

S. Cochran and D. Banner, 1977, "Spall Studies in Uranium," J. Appl. Phys. **48**, pp. 2729-2737.

D. C. Drucker, and W. Prager, 1952, "Soil Mechanics and Plastic Analysis or Limit Design," *Quart. Appl. Math.* **10**, pp. 157-175.

M. E. Kipp and R. J. Lawrence, 1982, "WONDY V - A One-Dimensional Finite-Difference Wave Propagation Code," Sandia National Laboratories report SAND81-0930.

Los Alamos National Laboratory, 1980, "LASL Shock Hugoniot Data," S. P. Marsh, editor (Univ. of Calif. Press, Berkeley).

J. M. McGlaun, 1991, "CTH Reference Manual: Cell Thermodynamics," Sandia National Laboratories report SAND91-0002.

J. M. McGlaun, S. L. Thompson, and M. G. Elrick, 1990, "CTH: A Three-Dimensional Shock Wave Physics Code," *Int. J. Impact Engrg.* **10**, pp. 351-360.

I. Nelson, 1977, "Constitutive Models for Use in Numerical Computations," in *Dynamical Methods in Soil and Rock Mechanics, Part 2, Plastic and Long-Term Effects in Soils*, edited by G. Gudehus, pp. 45-97.

W. A. Olsson, 1993, Internal communication.

Owens-Corning Fiberglas Corporation, 1990, "S-2 Glass Fiber - Enhanced properties for demanding applications," Pub. No. 15-PL-16154.

S. A. Silling, 1992, "Eulerian Simulation of the Perforation of Aluminum Plates by Nondeforming Projectiles," Sandia National Laboratories report SAND92-0493.

A. Vasudev and M. J. Mehlman, 1987, "A Comparative Study of the Ballistic Performance of Glass Reinforced Plastic Materials," *SAMPE Quarterly*, **18**, pp. 43-48.

ADVANCED MATERIALS

J. L. Wise and D. E. Cox, 1992, “Results of Impact-Response Studies on Aluminosilicate Glass,” Sandia National Laboratories Memorandum to G. F. Raiser, Brown University, October 15, 1992.

Distribution

External Distribution

Phillips Laboratory (3)
PL/WSSD
Kirtland AFB, NM 87117-6008
    Attn: F. Allahdadi
    Attn: D. Medina
    Attn: J. Thomas

Southwest Research Institute (4)
P.O. Drawer 28510
San Antonio, TX 78228-0510
    Attn: C. E. Anderson
    Attn: C. J. Kuhlman
    Attn: D. Littlefield
    Attn: J. D. Walker

Chen, Wing
FMC Corporate Technology Center
1205 Coleman Avenue
Santa Clara, CA 95050

U. S. Army ARDEC (2)
SMCAR-AEE-WW, Bldg. 3022
Picatinny Arsenal, NJ 07806-5000
    Attn: C. Chin
    Attn: E. Baker

Lockheed Missiles and Space Company (2)
Organization 89-10, Bldg. 157
P. O. Box 3504
Sunnyvale, CA 94088-3504
    Attn: Y. Choo
    Attn: E. Matheson

Chou, Dr. Shun-chin
Army Materials Technology Laboratory
SLCMT-MRD
Watertown, MA 02172-0001

Christiansen, Eric L.
NASA Johnson Space Center
Space Science Branch—Mail Code SN3
Houston, TX 77058

Christoph, George
Martin Marietta Laboratories
1450 S. Rolling Road
Baltimore, Maryland 21227

University of Colorado (2)
Department of Aerospace Engineering
Sciences
Campus Box 429
Boulder, CO 80309-0431
    Attn: R. Culp
    Attn: T. Maclay

Cykowski, Edward
Lockheed Engineering and Space Company
Mail Code B22
2400 NASA Road 1
Houston, TX 77058-3711

Fahrenthold, Eric P.
Department of Mechanical Engineering
The University of Texas
ETC 5.160
Austin, TX 78712

Thiokol Corporation (4)
P.O. Box 707
Brigham City, UT 84302-0707
    Attn: L. D. Ericksen, M/S 246
    Attn: L. Johnson, M/S 246
    Attn: K. E. Nielsen, M/S 246
    Attn: I. C. Swenson, M/S 280

Hill, Scott A.
NASA Marshall Space Flight Center
Mail Code ED52
MSFC, AL 35812-9000

U. S. Army Missile Command (2)
AMSMI-RD-ST-WF
Redstone Arsenal, AL 35898-5247
    Attn: S. D. Hill
    Attn: G. W. Snyder

Holsapple, Keith A.
Department of Aeronautics and Astronautics
FS10
The University of Washington
Seattle, WA 98195

Hough, Gary
Aerophysics Research Facility
P. O. Box 999
University of Alabama
Huntsville, AL 35899

Housen, Kevin
MS 87-60
The Boeing Company
PO Box 3999
Seattle, WA 98124

University of Florida (2)
Department of Aerospace Engineering,
Mechanics, & Engineering Science
231 Aerospace Building
Gainesville, FL 32611-2031
    Attn: C.-C. Hsu
    Attn: E. K. Walsh

Johnson, Gordon R.
Alliant Techsystems Inc.
600 2nd Street NE (MN11-2925)
Hopkins, MN 55343

U. S. Army Research Laboratory (17)
Attn.: AMSRL-WT-TC
Aberdeen Proving Ground MD 21005-5066
    Attn: G. Bulmash
    Attn: R. Coates
    Attn: J. Dehn
    Attn: Y. Huang
    Attn: K. Kimsey
    Attn: H. Meyer
    Attn: R. Mudd
    Attn: G. Philby
    Attn: J. Petresky
    Attn: G. Randers-Pehrson
    Attn: D. Scheffler
    Attn: S. Segletes
    Attn: G. Silsby
    Attn: M. N. Raftenberg
    Attn: W. R. Somsky
    Attn: B. Sorenson
    Attn: M. Zoltuski

Louie, N. A.
Department Y831, Mail Station 13-3
McDonnell Douglas Missile Space Systems
Company
MDSSC
5301 Bolsa Avenue
Huntington Beach, CA 92647

Miller, David M.
Owens-Corning Fiberglas Technical Center
Mail Stop 20-1
2790 Columbus Rd.
Route 16
Granville, OH 43023-1200

Moriaty, Thomas
Department of Engineering Sciences and
Mechanics
310 Perkins Hall
University of Tennessee
Knoxville, TN 37996-2030

Spitale, Guy
Jet Propulsion Laboratory
California Institute of Technology
Reliability Engineering Section
4800 Oak Grove Drive
Pasadena, CA 91109

Tanner, William G., Jr.
Space Sciences Laboratory
Baylor University, Dept. of Physics
PO Box 97303
Waco, TX 76798-7303

Tenenbaum, David A.
U. S. Army Tank Automotive Command
RD&E Center
AMSTA-RSS
Warren, MI 48397-5000

Williams, Larry
Martin Marietta
MP 126
Box 5837
Orlando, FL 32855

Los Alamos National Laboratory (3)
Mail Station 5000
P.O. Box 1663
Los Alamos, NM 87545
Attn: J. K. Dienes, MS B216
Attn: L. G. Margolin, MS D406
Attn: S. Sheffield, MS P952

Internal

0320	LDRD Office, 1011
0320	C. E. Meyers, 1011
0321	E. H. Barsis, 1400
1111	S. S. Dosanjih, 1402
0318	G. S. Davidson, 1403
0821	J. A. Ang, 1404
1110	R. C. Allen, Jr., 1405
1109	J. N. Jortner, 1408
1111	W. J. Camp, 1409
1110	E. F. Brickell, 1423
1109	A. L. Hale, 1424
0441	J. H. Biffle, 1425
0819	J. M. McGlaun, 1431
0819	K. G. Budge, 1431
0819	M. G. Elrick, 1431
0819	E. S. Hertel, 1431
0819	J. S. Peery, 1431
0819	S. V. Petney, 1431
0819	A. C. Robinson, 1431
0819	T. G. Trucano, 1431
0819	M. Wong, 1431
0820	P. Yarrington, 1432
0820	R. L. Bell, 1432
0820	R. M. Brannon, 1432
0820	H. E. Fang, 1432
0820	A. V. Farnsworth, 1432
0820	G. I. Kerley, 1432
0820	M. E. Kipp, 1432
0820	F. R. Norwood, 1432
0820	S. A. Silling, 1432 (20)
0820	P. A. Taylor, 1432 (20)
0821	P. L. Stanton, 1433
0821	M. B. Boslough, 1433
0821	L. C. Chhabildas, 1433
0821	D. E. Cox, 1433
0821	M. D. Furnish, 1433 (15)
0821	D. E. Grady, 1433
0439	D. R. Martinez, 1434
0827	J. S. Rottler, 1511
0832	H. S. Morgan, 1551
0437	R. K. Thomas, 1562
0437	D. E. Reedy, Jr., 1562
0515	S. T. Montgomery, 2561
0701	R. W. Lynch, 6100
1033	D. S. Drumheller, 6111
1033	J. C. Dunn, 6111
1033	J. L. Wise, 6111 (15)
0745	S. L. Thompson, 6418
0739	K. E. Washington, 6429
1151	M. Berman, 6515
1151	K. Boyack, 6515
9042	G. A. Benedetti, 8741
9042	P. E. Nielan, 8742
9042	A. McDonald, 8742
9043	M. L. Callabresi, 8743
9043	R. J. Kee, 8745
9043	C. M. Hartwig, 8745
9043	R. J. Kee, 8745
9044	W. A. Kawahara, 8746
9044	W.-Y. Lu, 8746
0899	Technical Library, 7141 (5)
9018	Central Technical Files, 8523-2
0619	Technical Publications, 7151
0100	Document Processing for DOE/OSTI, 7613-2 (10)

DATE
FILMED
6/17/94

END